Robust Design on Equal Channel Angle Extrusion of Ti-6Al-4V Using Taguchi Method

Dyi-Cheng Chen[1,*], Gow-Yi Tzou[2], Yi-Ju Li[1]

[1]Department of Industrial Education and Technology, National Changhua University of Education, Changhua 500, Taiwan
[2]Department of Mechanical and Automation Engineering, Kao Yuan University, Kaohsiung 821, Taiwan
*dcchen@cc.ncue.edu.tw

Abstract

This paper employs the rigid-plastic finite element (FE) DEFORM™ 3D software to investigate the plastic deformation behavior of Ti-6Al-4V titanium alloy during ECAE extrusion forming processing. Under various ECAE extrusion forming conditions, the FE analysis investigates punch load distribution and the effective strain distribution. A series of simulation analyses, in which the variables relied on different of the internal angle between the two die channels, the friction factors, the titanium alloy temperature and the strain rate of billet, were run to examine die radial load distribution when equal channel angle extrusion. Finally, we used the Taguchi method to determine the best design parameters. In the design process, our results confirmed the suitability of the FE method and the manufacturing process for titanium alloy forming.

Keywords

ECAE; Finite Element Analysis; Ti-6Al-4V Titanium Alloy; Effective Stain

Introduction

Rolling, extrusion and forging processes subject the working material to very high strains. The resulting plastic deformation causes a significant change in the physical and mechanical properties of the material. Thus, significant benefits can be gained by deforming metallic alloys utilizing some form of severe plastic deformation (SPD) technique. Segal *et al.* studied equal channel angular extrusion (ECAE) process or equal channel angular pressing (ECAP) method as a means of introducing large plastic strains of the billet. In the experiments, among them Markushev et al. used ECAE to produce 1560 aluminum alloy ultra-fine material, grain size up to 0.4 μm. Lee [5] used the upper-bound theory to deduce ECAE outside force and strain. In the finite element analysis, the software used based DEFORM-2D, only a few used the ANTARES and ABAQUS to analyze ECAE forming. Chen investigated into the plastic deformation behavior of billet with internal defective voids ECAE process. The paper combined with the number of Taguchi method to find the optimal parameters combination. Finally, it identifies the results of simulation analyses decreasing plastic deformation force behavior of Ti-6Al-4V titanium alloy during ECAE.

Analytical Theory

In accordance with plastic deformation process in ECAE has been studied analytically, a review of the literature used that the corresponding FE analyses have not been performed. Segal [1] showed that the strain induced in the billet is given by $\varepsilon = \left(2/\sqrt{3}\right)\cot(\phi/2)$ when ψ =0°. Iwahashi proposed the following general equation to describe the effects of ϕ and ψ on the induced strain, i.e. In ECAE, the initial velocity field is generated under the assumption that the billet is a linear viscous material.

2226-4523/15/01 001-6 © 2015 DEStech Publications, Inc.
doi:10.12783/ijmsci.2015.0501.01

$$\varepsilon = \left[\frac{2\cot\left(\frac{\phi}{2}+\frac{\psi}{2}\right)+\psi\cos ec\left(\frac{\phi}{2}+\frac{\psi}{2}\right)}{\sqrt{3}} \right] \quad (1)$$

Application of Taguchi Method

Taguchi parameter design method is to convert the signal quality characteristic noise ratio (Signal to Noise Ratio, S / N ratio), and thus the signal to noise ratio as a measure of quality characteristic indicator It can be used to represent the process or product quality and the degree of error factors. All manuscripts used the Taguchi method, a well-known robust-design technique, provides a comprehensive understanding of the individual and combined effects of various design parameters based on a minimum number of experimental trials. Taguchi method is actually required by the statistical ANOVA (Analysis of Variance, ANOVA) to strengthen the Taguchi method. The S/N ratio for the LB (lower is better) characteristics of the ECAE process is given by William & Creveling [15] and Belavendram as:

$$S/N = -10\log\left(\frac{1}{n}\sum_{i=1}^{n} y_i^2\right) \quad (2)$$

The equation n is the number of analysis repetitions under the same design parameter conditions, y_i explanated the obtained results, and subscript i explanated the number of design parameters arranged in the Taguchi orthogonal array.

Simulation Process Analysis

This study adopted the following assumptions: (1) the mold and die are all rigid bodies; (2) the ECAE workpiece is a rigid-plastic alloy material; (3) the friction factors among the workpiece, the extrusion die and ram remain are constant; and (4) the extrusion process occurs under isothermal conditions. This study adopted the shear friction equation for finite element simulation. Figure 1 presents a illustration of the ECAE of the present Ti-6Al-4V titanium alloy. Note that ϕ indicates the internal angle between the two flow channels, R_o is the outer arc between the two flow channels, and R_i is the inner arc between the two flow channels. The stress-strain relationship for the titanium alloy Ti-6Al-4V is summarized in Table 1.

Figures 2(a)~2(b) show the effective strain distribution in the Ti-6Al-4V alloy under different ECAE conditions. Furthermore, Figure 2(a) corresponds to ECAE conditions of ϕ=90°, m (friction ratio)=0.4, temperature of titanium alloy=900 °C, strain rate=0.01s^{-1}, and R_o=R_i=6mm. Similarly, Figure 2(b) corresponds to ϕ=135°, m=0.25, temperature of titanium alloy=1000 °C, strain rate=0.01 s^{-1}, and R_o=R_i=6mm. From the simulation that the maximum effective strains in Figures 2(a)~2(b) are 1.09 mm/mm and 0.441 mm/mm, respectively. The effective strain per pass, ε, is given by $\varepsilon = \frac{2}{\sqrt{3}}\cot\left(\frac{\phi}{2}\right)$, where ϕ is the internal angle between the two die channels. Hence, the effective strain per forming in Figures 2(a)~2(b) are calculated to be ε=1.15 mm/mm and ε=0.49 mm/mm, respectively.

Robust Design of ECAE

In the current study of the ECAE of Ti-6Al-4V titanium alloy, the principal characteristics of robust design are the axial direction Y axis-load (punch load) of the extruded product and a increased the robust design factor.

Design Factor

Table 2 shows the design parameters for the forming process of the ECAE that adopted the following design factors: Factor A: the internal angle between the two die channels, Factor B: the friction factor, Factor C: the temperature of the titanium alloy, and Factor D: the strain rate of billet. The remaining ECAE conditions were specified as R_o (outer arc of two die channels) and R_i (inner arc of two die channels).

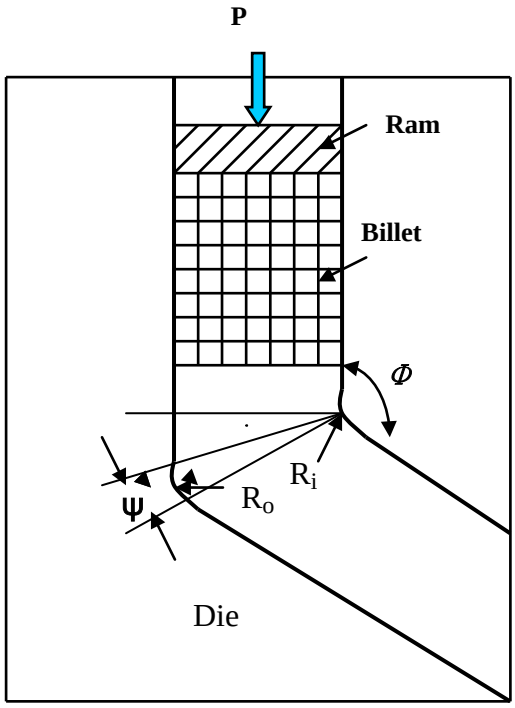

FIGURE 1. ILLUSTRATION OF ECAE PROCESS

TABLE 1. STRESS-STRAIN RELATIONSHIP OF TITANIUM ALLOY TI-6AL-4V

Flow Stress = f (Temperature, Strain Rate = 0.01s^{-1}, Strain) (MPa)

Strain--Tem.	800°C	900°C	1000°C
0	99.56	53.95	19.77
0.025	104.04	54.09	20.26
0.05	114.44	54.09	29.81
0.1	124.85	54.09	20.81
0.3	146.76	54.09	20.81
0.5	149.86	54.09	20.81

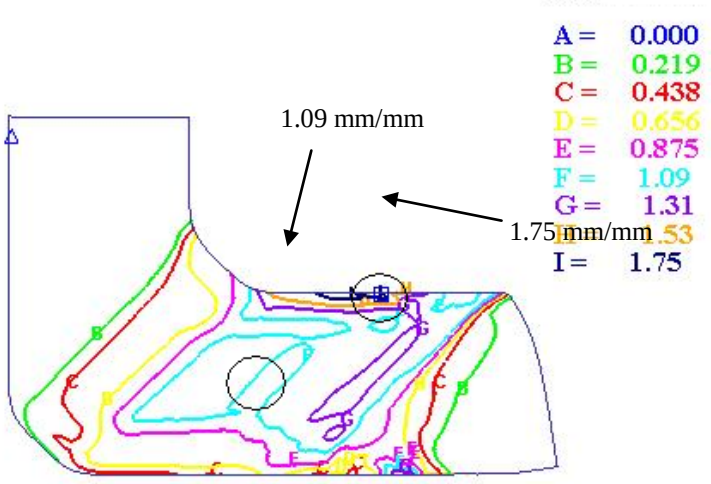

(a) ϕ (°)= 90, m (frictional ratio)=0.4, Ti(°C)=900, Strain rate (1/s)=0.01, R_o=R_i=6mm

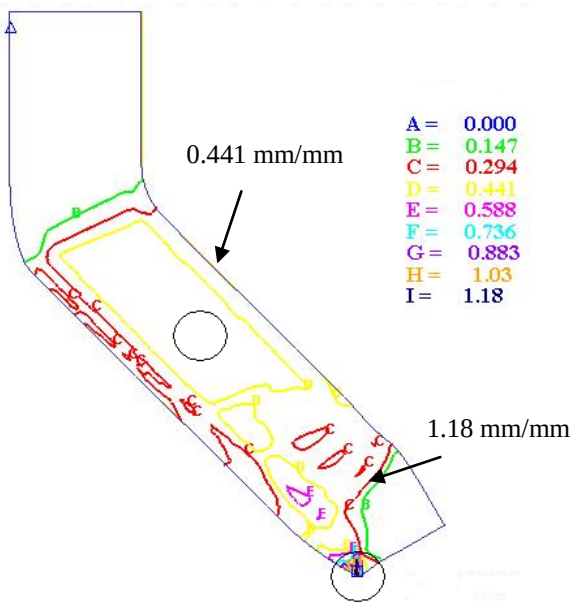

(b) ϕ (°)= 135, m (frictional ratio)=0.25, Ti(°C)=1000, Strain rate (1/s)=0.01, R_o=R_i=6mm

FIGURE 2. EFFECTIVE STRAIN OF TI-6AL-4V ALLOY UNDER DIFFERENT ECAE PROCESSING CONDITIONS

Analysis of Factor Response

From Tables 3 presents the S/N ratio response tables for die geometries of R_o=R_i=0mm. The factor response data presents in Figure 3. From Taguchi method calculation, a supposed is made that a larger S/N ratio indicates a made better forming condition. Furthermore, Figure 3 presents that for the die geometry of R_o=R_i=0mm, the optimal parameter settings are as follows: an internal angle between the two die and mold channels of 150° (design Factor *A3*), a friction factor of 0.1 (design Factor *B1*), a titanium alloy temperature of 1000°C (design Factor *C3*), and a strain rate of billet of 0.01s^{-1}(design Factor *D1*) for selected four factors and three level.

TABLE 2. EXPERIMENTAL CONFIGURATION TABLE IN TI-6AL-4V ECAE PROCESS (R_o=R_i=0MM)

Factors	Description	Level 1	Level 2	Level 3
A	ϕ (°)			
(Internal angle between the two die and mold channels)		120	135	150
B	m (friction ratio)	0.1	0.25	0.4
C	Ti(°C)(Temperature)	800	900	1000
D	Strain rate (1/s)	0.01	0.1	1

TABLE 3. S/N RATIO OF AXIS DIRECTION Y AXIS-LOAD (PUNCH LOAD) IN TI-6AL-4V ECA EXTRUSION PROCESS

Experiment No.	A	B	C	D	Y Load (kN), y1	Y Load (KN), y2	Average Y Load	S/N ratio
1	1	1	1	1	1.44	1.42	1.43	-3.11
2	1	2	2	2	1.08	1.10	1.09	-0.75
3	1	3	3	3	1.33	1.37	1.35	-2.61
4	2	1	2	3	1.39	1.40	1.40	-2.92
5	2	2	3	1	0.249	0.258	0.254	11.90
6	2	3	1	2	3.01	2.93	2.97	-9.46
7	3	1	3	2	0.239	0.237	0.238	12.47
8	3	2	1	3	2.78	2.87	2.83	-9.03
9	3	3	2	1	0.634	0.641	0.638	3.90
Mean of the total sum							1.36	0.043

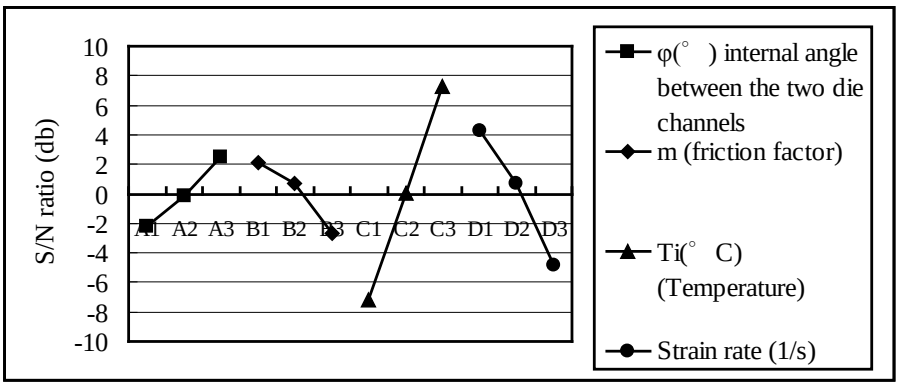

FIGURE 3. S/N RESPONSE GRAPH OF Y-LOAD (PUNCH LOAD)

Anova Statistical Analysis

The effects of the simulation trials were researched showing the analysis of variance analysis method. The results for the die and mold geometry cases of R_o=R_i=0mm is presented in Table 4. The high confidence (99%) and variance of Factors *A*, *B*, *C* and *D* indicate that the internal angle between the two die channels, the friction factor, the temperature of the titanium alloy, and the strain rate of billet have a significant influence upon the axis direction Y-load (punch load) of the ECAE extruded product. The confidence and significance are highly critical for control factors.

Confirmation Optimal Design Parameters

Accordingly, a simulation was performed using the optimal design parameter combination for the die geometry of R_o=R_i=0 mm in selected four factors and three level, i.e. *A3B1C3D1*. The results indicated that the axis direction Y axis-load (punch load) of the new design was 0.138 kN with a S/N value of 17.20 (dB).

TABLE 4. AXIS DIRECTION Y-LOAD (PUNCH LOAD) ANALYSIS OF VARIANCE (ANOVA)

Factor	Description	SS	DOF	Variance	F	Confidence	Significant?*
A	ϕ (°) (angle)	0.3197	2	0.15985	301.6	100%	Yes
B	m (friction ratio)	1.2145	2	0.60725	1145.8	100%	Yes
C	Ti(°C)(Temperature)	10.5570	2	5.2785	9959.4	100%	Yes
D	Strain rate (1/s)	3.5924	2	1.7962	3389.1	100%	Yes
	Error	0.0048	2	0.00053			
	Total	15.6884	17		*Note: At least 99% confidence		

Conclusions

This study implements a series analysis to research the Ti-6Al-4V during equal channel angular extrusion (ECAE). The analysis has displayed that:

(1) the internal angle between the two die channels, the friction factor, the temperature of the titanium alloy, and the strain rate of billet have a significant influence upon the axis direction Y-load (punch load) of the ECAE extruded product.

(2) the flow channels ϕ=90°, has maximum effective strains result.

The simulative analysis results verified the utility of the Taguchi design means in optimizing the ECAE forming for the titanium alloy.

REFERENCES

[1] V. M. Segal. “Equal channel angular extrusion: from macromechanics to structure formation.” Materials Science and Engineering A 271 (1999):322-333.

A. Shan, I. G. Moon, H. S. Ko, and J. W. Park. "Direct observation of shear deformation during equal channel angular pressing of pure aluminium." Scripta Materials 41(4) 1999:353-357.

[2] S. L. Semiatin, P. B. Berbon, and T. G. Langdon. "Deformation heating and its effect on grain size evolution during equal channel angular extrusion." Scripta Materials 44 (2001):135-140.

[3] M. V. Markushev, M.Yu. Murashkin, P. B. Prangnell, A. Gholinia, and O. A. Maiorova. "Structure and mechanical behavior of an Al-Mg alloy after equal channel angular extrusion." NanoStructured Materials 12 (1999): 839-842.

[4] D. N. Lee, "An upper-bound solution of channel angular deformation. " Scripta Materials 43 (2000): 115-118.

[5] S. L. Semiatin, D. P. Delo, and E. B. Shell. "The effect of material properties and tooling design on deformation and fracture during equal channel angular extrusion." Scripta Materials 48 (2000):1841-1851.

[6] J. R. Bowen, A. Gholinia, S. M. Roberts, and P. B. Prangnell. "Analysis of the billet deformation behavior in equal channel angular extrusion." Materials science and Engineering A 287 (2000):87-99.

[7] L. Zuyan, L. Gang, and Z. R. Wang. "Finite element simulation of a new deformation type occurring in changing-channel extrusion." Journal of Materials Processing Technology 102 (2000): 30-32.

[8] H. S. Kim. "Finite element analysis of equal channel angular pressing using a round corner die." Materials science and Engineering A 315 (2001):122-128.

[9] R. Srinivasan. "Computer simulation of the equal channel angular extrusion (ECAE) process." Scripta Materials 44 (2001): 91-96.

[10] D. C. Chen and C. P. Chen. "Investigation into equal channel angular extrusion process of billet with internal defects." Journal of Materials Processing Technology 204 (2008): 419-424.

[11] Y. Iwahashi, J. Wang, Z. Horita, M. Nemoto and T. G. Langdon. "Principle of equal-channel angular pressing for the processing of ultra-fine grained materials." Scripta Materialia 35(2) (1996): 143-146.

[12] W. C. Hsu and T.Y. Yu. "Support vector machines parameter selection based on combined Taguchi method and staelin method for E-mail spam filtering." International Journal of Engineering and Technology Innovation 2(2) (2012): 113-125.

[13] L. K. Wang, J. Y. Shieh, K. H. Lin and K. Huang. "A two-stage Taguchi design example-image quality promotion in miniature camera/cell-phone lens." International Journal of Engineering and Technology Innovation 2(3) 2012: 163-171.

[14] W.Y. William and C.M. Creveling: Engineering methods for robust product design, Addison-Wesley, Boston, 1998.

[15] N. Belavendram: Quality by design, Prentice-Hall, New York, 1995.

Dyi-Cheng Chen is a Professor in the Department of Industrial Education and Technology at National Changhua University of Education, Taiwan. During the school, he implement many researches works. He is interested in technological and vocational education, mechanical engineering and material forming areas.

Gow-Yi Tzou is a Professor in the Department of Mechanical and Automation Engineering, Kao Yuan University, Taiwan. During the school, he implement many researches works. He is interested in mechanical engineering and material forming areas.

Yi-Ju Li is a full time Student in the Department of Industrial Education and Technology at National Changhua University of Education, Taiwan. He is interested in technological and vocational education, mechanical engineering.

Mechanical and Three-Body Abrasive Wear Behaviour of Cenosphere Filled Epoxy Composites

B. Suresha[1*], A. Chandrashekar[2], S. Srinivas[3]

[1]Department of Mechanical Engineering, The National Institute of Engineering, Mysore-570 008, INDIA

[2]Department of Mechanical Engineering, Hirasugar Institute of Technology, Nidasoshi-591236, Belgaum, INDIA

[3]Quality Assurance, Brakes India Limited, Sundaram Polymer Division, Nanjangud-571302, India

[*1] sureshab2004@yahoo.co.in; [2]chandrashekar_dev@yahoo.co.in; [3] srinivas.s@brakesindia.ac.in

Abstract

Novel epoxy composites made from major industrial waste, fly ash cenosphere (FA-ceno) particles have been developed. The effect of FA-ceno loadings on mechanical and three-body abrasive wear behaviour has been investigated. The tribological behaviour of three-body abrasive wear tests with different loads/abrading distances were performed at room temperature by using a Rubber wheel abrasion apparatus. Experimental results showed that the tensile strength and Young's modulus of FA-ceno filled epoxy are more than those of neat epoxy. The wear volume increased with increasing abrading distance and the specific wear rate decreased with increasing abrading distance/ load which depends on filler loading. Among the filled composites tested, 10 wt% silane treated with FA-ceno filled epoxy showed a promising trend. Finally, the scanning electron microscopic observation on the wear mechanisms of epoxy and their composites were discussed.

Keywords

FA-Ceno Filled Epox; Mechanical Properties; Specific Wear Rate; Worn Surface Morphology

Introduction

Fly ash is a coal combustion by-product consisting primarily of aluminosilicates. It gives better performance at a lower cost. Its application areas include brick manufacturing, partial replacement of cement, in land filling and reclamation of land, as soil fertilizer, etc. Along with these, extensive research is going on to utilize the fly ash as filler in polymer matrix composites. Table 1 shows the typical chemical composition of fly ash. Fly ash cenospheres (FA-ceno) are hollow aluminum silicate micro-spheres obtained from the fly ash of coal fired thermal power plants. FA-ceno into polymer matrix reduces the consumption of the resin material and increases the bulk properties of composites. FA-ceno particles are extremely attractive as reinforcing agents because of their remarkable elastic modulus and abrasion resistance. In addition, they may yield an improved interface between matrix and particles with respect to the more conventional ceramic reinforcements [1].

TABLE 1 TYPICAL CHEMICAL COMPOSITION OF FLY ASH IN WEIGHT PERCENT [2]

Al_2O_3	SiO_2	MgO	Fe_2O_3	TiO_2	CaO	Na_2O	K_2O	Others
30. 3	54.3	1.9	7.5	1.8	1.5	1.1	2.1	1.4

Among the various engineering materials, polymers are widely considered as an important group of materials due to their low density, ability to undergo large inelastic deformation, and easy processability. However, low stiffness, high wear rate, and low hardness limit their usage in various demanding tribological applications. Hence, a new approach of materials designed with tailor-made properties is attempted to develop particulate filled polymer composites.

Polymeric materials are filled by inorganic fillers to improve the mechanical, electrical, thermal, optical, and processing properties. A judicious selection of matrix and the reinforcing phase can lead to a composite with a combination of strength and modulus comparable to or even better than those of conventional materials [3]. Among more than 100 different types of organic and inorganic reinforcing materials researched and reported in the

2226-4523/15/01 007-9 © 2015 DEStech Publications, Inc.
doi:10.12783/ijmsci.2015.0501.02

literature, only a few fillers like carbon black, mica, silicon carbide, alumina and graphite, have been commercialized and used extensively [4,5].

The physical and mechanical characteristics can further be modified by incorporating solid filler phase to the matrix during the composite preparation. Liau et al. [6] found a significant improvement in impact energy of hybrid composites incorporating either particulates or ceramic whiskers. Hard particulate fillers consisting of ceramic or metal particles and fiber fillers made of glass are being used these days to dramatically improve the wear resistance of composites, even up to three orders of magnitude [7]. More recently, a number of investigations into the behaviour of cenospheres filled polymer systems have been reported [8,9]. Of particular interest to this current study is the work of Cardoso et al. [10] which investigated the behaviour of cenospheres in a thermosetting polyester matrix. The study investigated the effect of particle size and surface treatments on a range of mechanical properties including elastic modulus, compressive strength and fracture toughness. Rohatgi [11] reported that with the increase in volume percentage of fly ash, hardness increases in aluminum-fly ash composites. Some researchers have reported their findings on fly ash filled polymer matrix composites [12–19]. Most of the studies reported are based on the mechanical, thermal, and electrical behavior of fly ash filled polymer matrix composites and a few reports are also available on the wear characteristics of such composites. Kulkarni and Kishore [20] discussed the effect of contact at the interface on compression properties of fly ash filled epoxy composites. They found that the silane treated with fly ash filler in epoxy yielded the best compression strength than that the corresponding untreated composites did. Ramakrishna et al. [21] investigated the effect of fly ash content on compression and impact strength of toughened epoxy composites. Srivastava et al. [22] examined the tensile and fractured properties of fly ash incorporated epoxy composites and concluded that the tensile strength decreased and the modulus of elasticity increased with increase in fly ash content.

Abrasive wear can occur as two-body abrasion, three-body abrasion, or a combination thereof [23]. To understand the low-stress abrasive wear mechanisms of particulate filled polymeric composites, mechanism of its metallic or ceramic counter part needs to be addressed. It is therefore necessary to understand the basic phenomenon of three-body abrasion. Sole et al. [24] studied the effect of minerals fillers such as talc, $CaCO_3$, $BaSO_4$, and fly ash on abrasive wear resistance of polypropylene (PP). They investigated the wear resistance of three types of composite materials containing epoxy resin matrix, epoxy filled with silica and epoxy filled with tungsten carbide particles and observed that the matrix filled with the tungsten carbide had highest value of wear resistance in more severe wear conditions. Thus, it can be seen from the literature that abrasive wear behaviour of polymer and their composites are complex and it is widely recognized that the abrasive wear behaviour in polymers are not well understood.

Epoxy resins are used in coating industry as surface coating materials which combine toughness, adhesion and good chemical resistance. In addition, epoxy resin can also be used in both molding and laminate techniques to make fiber and/filler reinforcement with better mechanical strength, chemical resistance and electrical insulating properties. This is due to the competency of epoxy resin that shows good adhesion to the embedded fiber/filler.

In spite of this, not much is reported on this aspect except in the case of abrasive wear performance of the same composites by the authors. Moreover, no paper could be available that reports on the effect of FA-ceno contents on the abrasive wear behaviour. Hence, an attempt has therefore been made to study the mechanical and three-body abrasive wear behavior of FA-ceno filled epoxy composites. The wear behavior has been quantified in terms of the wear volume and specific wear rate. The different wear mechanisms were also reported.

Experimental Details

Materials and Silane Tretament

The composite material investigated in the present study, consists of LY 556 epoxy resin with HY951 grade room temperature curing hardener with diluent DY 021 (all supplied by Hindustan Ciba Geigy). The filler material is fly ash cenosphere (FA-ceno) of particle size in the range 30-50 μm used in the present study. The FA-Cenospheres were purchased from Ashtech (India) Pvt. Ltd. Mumbai, Maharashtra, India. 3-Amino propyl triethoxy silane (APTS) was obtained from Sigma Aldrich (USA) and dibutyl maleate (DBM) and all other solvents were obtained

from S.d. Fine Chemicals, Mumbai, India.

Silane grafted FA-Cenospheres was synthesized grafting APTS onto FA-Cenospheres. The grafting reaction was carried out in a mixture of water/ethanol (20:80 wt%). A quantity of 50 g of FA-Cenospheres was first introduced into the mixture of water/ethanol and the temperature was kept at 80 ^{0}C. Further, 2% by volume of APTS was added into the aforementioned solution and continuously stirred for 5 h at 80 ^{0}C. This resultant mixture was filtered and washed many times using mix of water/ethanol and dried using hot air oven.

FIGURE 1. MULTIPLE CAVITY MOULD FOR FABRICATION OF FA-CENO FILLED EPOXY SLABS.

Fabrication

As regards the processing, a multiple cavity steel mould, shown in Figure 1, was fabricated and a Teflon sheet was placed, over which neat epoxy resin mixed with hardener in the ratio 100:12 by weight was poured slowly. The mold plates were coated with release agent in order to aid the ease of separation of cast slab after curing. The filled mold was cured for a day at room temperature. The slabs prepared were measured 200 mm x 100 mm x 5.5 mm by size. To prepare the FA-ceno filled epoxy composites, besides the epoxy hardener mixture, a required amount of filler by wt% was included to form the resin mix. Abrasion test samples of size 75 mm x 25 mm x 5.5 mm were prepared from the cured sheet using abrasive cut-off machine. The composites selected for the present study are listed in Table 2.

TABLE 2 COMPOSITES SELECTED FOR THE PRESENT STUDY

Material (designation)	Matrix (wt%)	Filler (wt%)
Neat Epoxy (Ep)	Epoxy (100)	----
Fly ash cenosphere-Epoxy (3FA-ceno-Ep)	Epoxy (97)	Fly ash cenosphere (3)
Fly ash cenosphere-Epoxy (6FA-ceno-Ep)	Epoxy (94)	Fly ash cenosphere (6)
Fly ash cenosphere-Epoxy (10FA-ceno-Ep)	Epoxy (90)	Fly ash cenosphere (10)

Testing

1) Mechanical Testing

The mechanical properties such as tensile and flexural properties were investigated using Universal tensile testing machine (JJ Lloyd, London, United Kingdom, capacity 1–20 kN) in accordance with ASTM D 638 and ASTM D790 respectively. The tensile test was performed at a crosshead speed of 5 mm/min. Five samples were tested for each composition of the composites.

2) Rubber Wheel Abrasion Test

A Rubber wheel abrasion tester was (as per ASTM G- 65) used for three-body wear tests. Samples of size 75 mm x 25 mm x 5.5 mm were used. The test details are listed in Table 3. The sample was initially weighed to an accuracy of 0.0001g in an electronic balance. Densities of the composites were determined using a high precision electronic balance (Mettler Toledo machine Model AX 205) following the Archimedes principle. The wear was measured by the loss in weight, which was then converted into wear volume using the measured density data. The specific wear rate (Ks) was calculated from the equation:

$$K_S = \frac{\Delta V}{L \times D} \quad m^3 / Nm \tag{1}$$

where, ΔV is the volume loss, L is the load and D is the abrading distance. After wear test, the worn surfaces of specimens were examined using a scanning electron microscope (JSM 840A model of JEOL make). Before the examinations, a thin gold film was coated on the worn surface by sputtering to achieve a conducting layer.

TABLE 3 THREE-BODY WEAR TEST CONDITIONS

Parameters	Experimental conditions	
Normal load (N)	24	36
Speed (RPM)	200 ±5	200 ±5
Abrading distance (m)	150-600	150-600
Abrasives (200-250 μm)	Silica sand	Silica sand

Results and Discussion

Mechanical Properties

1) Tensile Properties

Under tensile loading conditions, particles are the primary load bearing phase in the composite. Perfect bonding between particles and matrix leads to higher stress-transfer under tensile loading. In this study, the silane surface treatment is given to the FA-ceno particles in order to have good particle–matrix interfacial strength so that a direct tension of the effect of spherical particle and wt% on the epoxy composite can improve the tensile strength and modulus of the composites.

The mechanical properties of FA-ceno filled epoxy composites are listed in Table 4. It can be seen that incorporation of silane treated with FA-ceno is slight increase in tensile strength and modulus of the epoxy composites. This phenomenon can be attributed to the strong and weak interactions between the polymer and FA-ceno particles. Formation of fine silica particles in the vicinity of FA-ceno particles can be observed. These fine particles can greatly improve the epoxy- FA-ceno interactions, thereby leading to better mechanical properties. In the experimental range, the best mechanical properties were obtained with the composite having 10 wt% of FA-ceno treated with silane coupling agent. Inclusion of FA-ceno into epoxy decreases the strain as expected.

TABLE 4 MECHANICAL PROPERTIES PARTICULATE FILLED EPOXY COMPOSITES

Samples	Tensile strength (σ) MPa	Young's modulus (MPa)	Flexural strength (σ) MPa	Flexural modulus (MPa)
Ep	81.42	3457	30.2	777.99
3FA-ceno-Ep	85.97	4659	24.52	640.62
6FA-ceno-Ep	94.67	4886	22.42	600.68
10FA-ceno-Ep	97.54	5124	20.64	580.81

2) Flexural Properties

The modification of the mechanical properties of epoxy matrix modified by the addition of FA-ceno depends on many parameters. Adding some FA-ceno particles can enhance the properties but adding more FA-ceno particles may not guarantee more improvement. This is due to the increase in viscosity of the epoxy on the inclusion of FA-ceno and the increase of voids during the mixing stage.

The test results for flexural strength and modulus are also listed in Table 4. It is seen that in all the FA-ceno filled epoxy samples the flexural strength of the composite decreases with increase in filler content. The neat epoxy has strength of 30.2 MPa in flexure and it may be seen from the table that this value drops to 24.52 MPa with FA-ceno of 3 wt%. In this study, the inclusion of FA-ceno causes maximum reduction in the composite flexural strength. There can be two reasons for this decline in the strength properties of these particulate filled composites compared to the neat ones. One possibility is that the chemical reaction at the interface between the filler particles and the matrix may be too weak to transfer the flexural stress; the other is that the corner points of the irregular shaped particulates result in stress concentration in the epoxy matrix. These two factors are responsible for reducing the flexural strength of the composites so significantly. The compatibility of FA-ceno particles in epoxy matrix seems to be not good and as a result of which the percentage reduction in flexural

strength is highest. The flexural moduli of these filled composites 3, 6 and 10 wt% FA-ceno, are also found to be less than that of neat epoxy.

Three-Body Abrasive Wear Behaviour

1) Wear Volume

Figures 2(a) and (b) show the wear volume loss with abrading distance for different loads. It is evident from these figures that irrespective of the type samples used, there is a near linear trend of wear volume loss which strongly depends on the load and abrading distance. From Figures 2(a) and (b), it can be observed that, irrespective of the FA-ceno content, there is a continuous increase in wear volume values with increasing abrading distance. However, the intensity of this decrease is marginal with increase in FA-ceno content. This can be attributed to the domination of the brittleness of the epoxy matrix due to the addition of filler. The neat epoxies exhibited considerably higher wear volume than that of FA-ceno filled epoxy composites. The composite with FA-ceno as filler was found to be much more wear resistant than that of neat epoxy. By increasing the load from 24 to 36 N, the wear volume of neat epoxy increased from 0.101 x 10^3 to 0.154 x 10^3 mm^3 as compared with FA-ceno filled epoxy (10 wt%), whose wear volume increased from 0.0357x 10^3 to 0.1 x 10^3 mm^3. The lowest wear volume loss is seen with 10 wt% FA-ceno filled epoxy composite. The wear volume loss is lower in FA-ceno filled epoxy as compared with neat epoxy indicating higher matrix-filler interaction in FA-ceno filled epoxy composites.

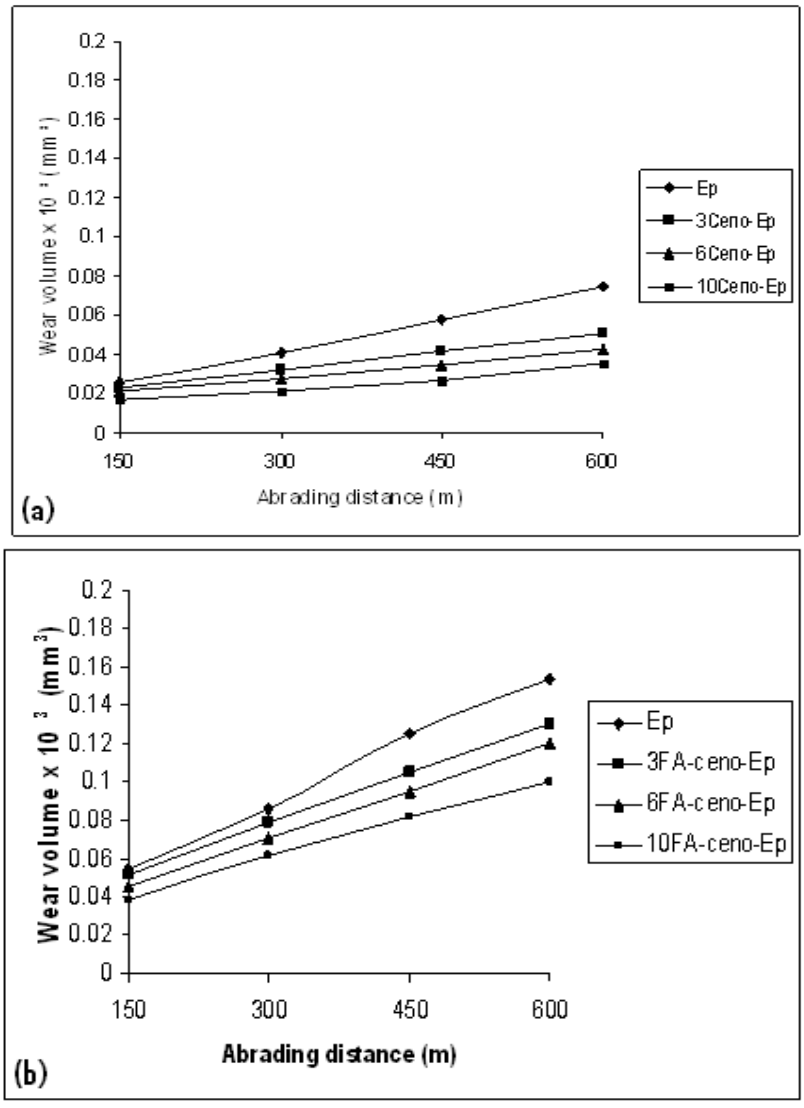

FIGURE 2. WEAR VOLUME AS A FUNCTION OF ABRADING DISTANCE OF UNFILLED AND FA-CENO EPOXY COMPOSITES AT; (A) 24 N AND (B) 36 N.

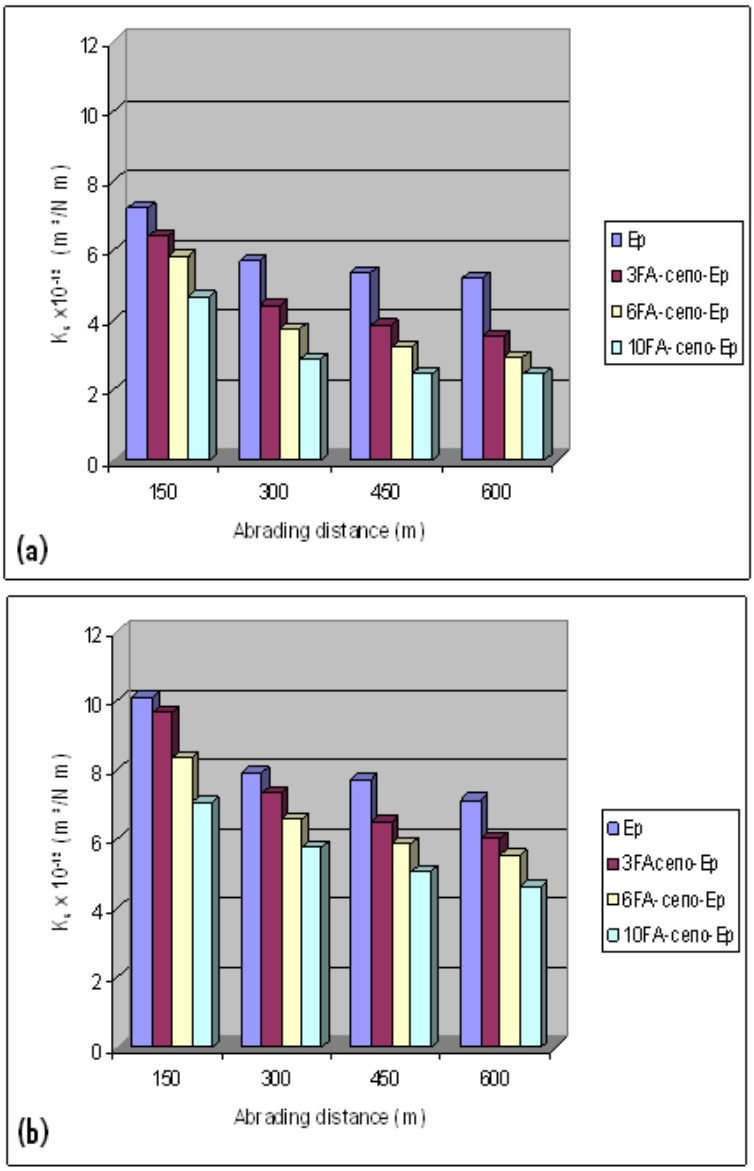

FIGURE 3. SPECIFIC WEAR RATE AS A FUNCTION OF ABRADING DISTANCE OF UNFILLED AND FA-CENO EPOXY COMPOSITES AT; (A) 24 N AND (B) 36 N.

2) *Specific Wear Rate*

The results of specific wear rate as a function of abrading distance of neat epoxy and their composites are shown in Figures 3(a) and (b) respectively. For all the composites tested, it is observed that the specific wear rate decreases with increase in filler content. At all abrading distances, the highest specific wear rate is for neat epoxy with a value of 12.04 x 10^{-12} m^3/Nm and the lowest value of 7.04 x 10^{-12} m^3/Nm for 10 wt% FA-ceno filled epoxy composite. This is attributed to the fact that, in 10 wt% silane treated with FA-ceno filled epoxy composite, the dispersion of filler is more uniform and better adhesion with the epoxy matrix. Initially the specific wear rate is very high and reaches an almost steady state with increase in filler wt%. Furthermore, the specific wear rate decreases with increase in filler content. The specific wear rate strongly depends on the applied load and abrading distance for all the samples. Among the composites studied, the abrasion resistance is better for 10 wt% FA-ceno filled epoxy composites.

3) *Worn Surface Morphology*

Material microstructure plays an important role in determining the active wear mechanism in polymer matrix composites. Scanning electron microscopy studies seem to support the difference in wear behaviour observed under different experimental conditions.

Scanning electron micrograph (SEM) of neat epoxy and FA-ceno filled epoxy composites subjected to 36 N load and 600 m abrading distance is displayed in Figure 4. The worn surface shows the formation of wear tracks by plowing. It can be seen from Figure 4 that the neat epoxy surface exhibits irregular-shaped distributed debris due to the actions of abrasive involving plastic deformation and scratching owing to ploughing. The worn surface of neat epoxy shows severe matrix damage and more cracks throughout the sample surface.

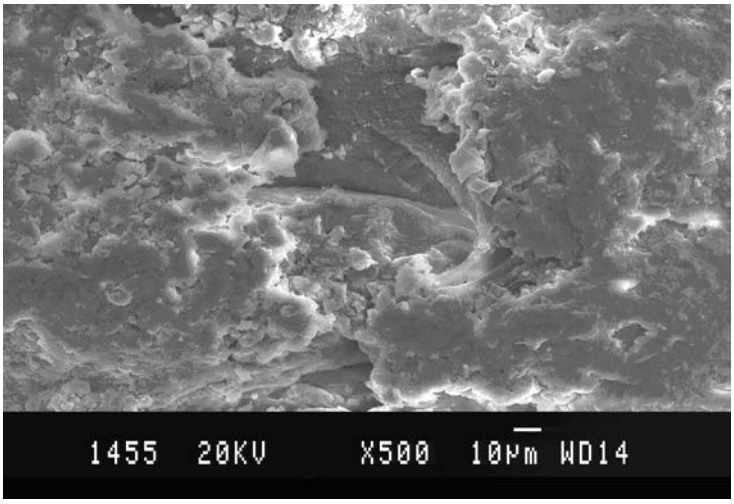

FIGURE 4. SEM PICTURE SHOWING WORN SURFACE FEATURES AT 36 N FOR NEAT EPOXY..

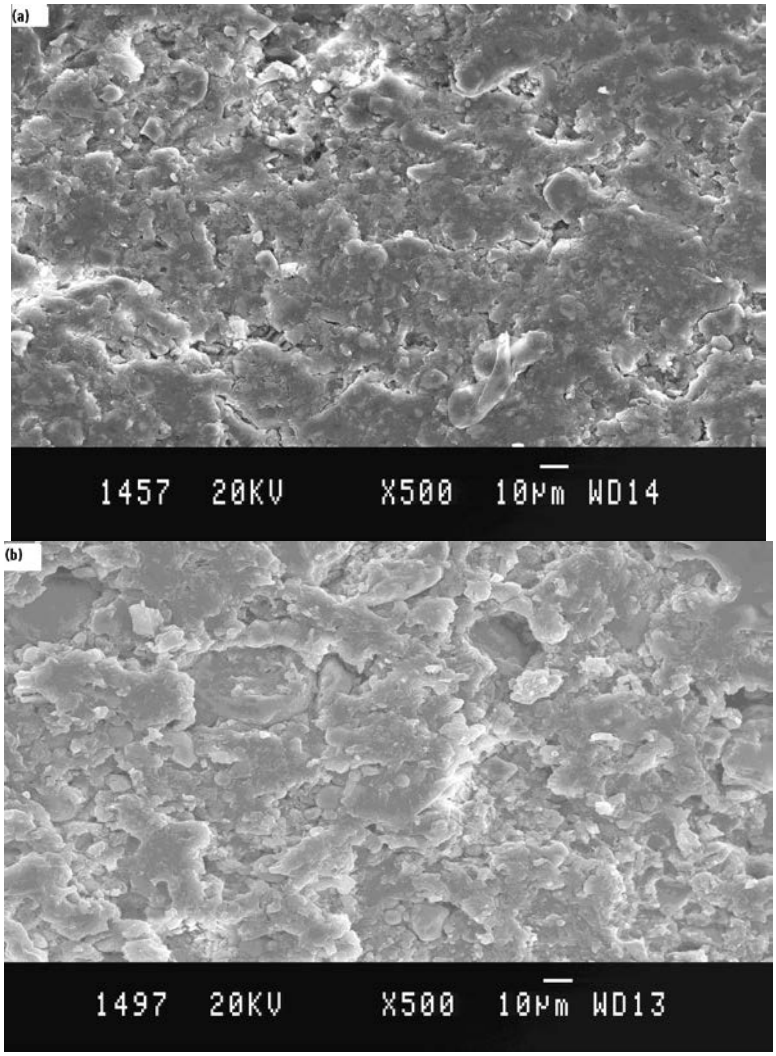

FIGURE 5. SEM PICTURES SHOWING WORN SURFACE FEATURES AT 36 N FOR (a) 3 WT% FA-CENO-EP AND (b) 10 WT% FA-CENO -EP COMPOSITES.

SEM photomicrographs, Figures 5(a) and (b), pertain to the worn surface features of 3 and 10 wt% FA-ceno filed epoxy composites. For FA-ceno filled epoxy, when it is abraded under the same test conditions, less matrix wear occurs ; however, the protruding filler particles were rounded off and showed evidence of scratching, cracks at some regions and chipping. Development of cracks in epoxy can cause the removal in the form of matrix filler debris because of the debonding between epoxy and cenosphere and the brittle nature of epoxy, FA-ceno particles which are clearly visible in Figures 5(a) and (b). These figures show less matrix wear and less distortion when compared with neat epoxy. The hard FA-ceno filler in epoxy impedes the crack propagation during the abrasion process. This may be the reason for improving wear resistance in filled epoxy composite. It is reported in the literature [25-27] that most of the filled composites, which show better performance in sliding wear, exhibit poor abrasion resistance, whereas FA-ceno filled epoxy composites exhibit improved abrasion resistance.

Conclusions

Effect of silanated FA-ceno particles on mechanical and abrasive wear behaviour of epoxy composites is experimentally characterized. The followings are the salient observations made from the present investigation:

- A continuous increase and marginal decrease in the tensile and flexural properties with increasing FA-ceno concentrations have been observed in epoxy composites. The tensile properties are enhanced by the presence of silanated FA-ceno particles because matrix fracture plays a greater role in deformation and fracture of the composite under tensile loading.
- The FA-ceno particles can be used as filler in polymer matrix composites to produce low cost new materials for uniaxial loading applications.
- Differing trends in abrasive wear volume were seen for unfilled and FA-ceno filled epoxy composites.
- The abrasive wear volume strongly depends on the applied load and abrading distance for all the composites.
- 10 wt% of FA-ceno filler in epoxy shows good performance to the three-body abrasive wear.
- SEM observations of silane treated with FA-ceno filled epoxy shows better filler matrix interaction as compared with neat epoxy.
- Worn surfaces indicate plowing, cracking at the interface, and particle pullout.

ACKNOWLEDGMENT

We would like to thank N. Govinda Raju, Chief Executive Officer, Magnum Engineers, Bangalore, for providing the testing facilities. The authors are thankful to the Management and Principal Dr. G.L, Shekar, The National Institute of Engineering, Mysore, India, for their encouragement.

REFERENCES

[1] Rohatgi, PK, Huang P, Guo R, Keshevaram BN, Golden D. in: Malhotra VM, (Ed.), Proceedings of the 5th CANMET/ACI International Conference on Fly Ash Silica Fume Slag and Natural Pozzolans in Concrete. American Concrete Institute, Detroit, MI, 1995: 459.

[2] Meyers, James, F., Raman Pichumani, and Bernadette, S. Kapples. (1976). Fly Ash: A Highway Construction Material. Federal Highway Administration, Report No. FHWA-IP-76-16, Washington, DC.

[3] Jang, B.Z. (1994). Advanced Polymer Composites: Principles and Applications. ASM International, Materials Park, Ohio, USA.

[4] Pukanszky, B. (995). Particulate Filled Polypropylene: Structure and Properties. in: Karger-Kocsis, J. (ed.), Polypropylene: Structure, Blends and Composites. Chapman & Hall, London,: pp. 1–70.

[5] Kenny, J.C., McBriety ,V.J., Rigbi. Z. and Douglass, D.C. (1991). Carbon black filled natural rubber. 1. Structural

investigations, Macromolecules, **24()**: 436–443.

[6] Liau, J.Y., Jang, B.Z., Hwang, L.R. and Wilcox, R.C. (1988). Toughening composites by matrix modification, Plastics Engineering, **44**: 33–37.

[7] Gregory ,S.W., Freudenberg, K.D., Bhimaraj, P. and Schadler, L.S. (2003).. A Study on the Friction and Wear Behavior of PTFE Filled with Alumina Nanoparticles, Wear **254**: 573–580.,

[8] Parameswaran, V. and Shukla, A. (2000). Processing and characterization of a model functionally gradient material. Journal of Materials Science, **35**: 21-29.

[9] Chalivendra, V.B., Shukla, A., Bose, A. and Parameswaran, V. (2003). Processing and mechanical characterization of lightweight polyurethane composites, Journal of Materials Science, **38**: 1631-1643.

[10] Cardoso, R.J., Shukla, A. and Bose A. (2002). Effect of particle size and surface treatment on constitutive properties of polyester-cenosphere composites, Journal of Materials Science, **37**: 603-613.

[11] Rohatgi, P.K. (1994). Low-cost fly-ash-containing aluminum–matrix composites, Journal of Materials, **46**: 55–59.

[12] Ramakrishna, H.V., Padma Priya, S.and Rai, S.K. (2005). Tensile and flexural properties of unsaturated polyester/granite powder and unsaturated polyester/fly ash composites, Journal of Reinforced Plastics & Composites, **24**: 1279–1287.

[13] Kishore, S.S. (2005). Impact studies in elastomer, fly ash, and hybrid filled epoxy composites: comparison of data and fracture features of the samples cured via a single room temperature and multiple high temperatures, Journal of Reinforced Plastics & Composites, **24**: 1013–1024.

[14] Kishore, S.S. (2005). Individual and combined roles of CTBN and fly ash in epoxy system under compression: correlation between microscopic features and mechanical behaviour, Journal of Reinforced Plastics & Composites, **24**: 299–312.

[15] Bose, S. and Mahanwar, P.A. (2004). Effect of fly ash on the mechanical, thermal, dielectric, rheological and morphological properties of filled nylon 6. Journal of Minerals Materials Characterization & Engineering, **3**: 65–72.

[16] Sen, S. and Nugay, N. (2000). Uncured and cured state properties of fly ash filled unsaturated polyester composites, Journal of Applied Polymer Science, **77**: 1128–1136.

[17] Sombatsompop, N. Thongsang, S. Markpin, T. and Wimolmala, E. (2004). Fly ash particles and precipitated silica as fillers in natural rubber and styrene–butadiene rubber compounds, Journal of Applied Polymer Science, **93**: 2119–2130.

[18] Ray, D., Bhattacharya, D,, Mohanty, A,K., Drzal, L.T. and Misra, M. (2006). Static and dynamic mechanical properties of vinyl ester resin matrix composites filled with fly ash, Macro Mater Eng, **291**: 784–792.

[19] Dipa, Ray. and Gnanamoorthy, R. (2007). Friction and wear behavior of vinyl ester resin matrix composites filled with fly ash particles, Journal of Reinforced Plastics & Composites, **26**:5-13.

[20] Kulkarni, S.M.and Kishore. (2002). Effect of contact at the interface on the compressive properties of fly ash-epoxy composites, J Adhesion, **78**: 155-166.

[21] Ramakrishna, H.V., Padma Priyam S., Rai, S.K. and Varadarajulu, A. (2005). Studies on tensile and flexural properties of epoxy toughened with PMMA/granite powder and epoxy toughened with PMMA/fly ash composites. Journal of Reinforced Plastics & Composites, **24**:1269–1277.

[22] Srivastava, V.K. and Shembekar, P.S. (1990). Tensile and fracture properties of epoxy resin filled with fly ash particles, Journal of Materials Science, **25**: 3513-3516.

[23] Hutchings, I.M. (1992). Tribology, CRC Press, London, pp. 156-162.

[24] Sole, B.M. and Ball, A. (1996). On the abrasive wear behavior of mineral filled polypropylene, Tribology International, **29**: 457–465.

[25] Chand N, Gautam KKS. Influence of load on abrasion of fly ash–glass fiber reinforced composites. J Mater Sci Lett 1994;13:230–233.

[26] Chand N, Nayak A, Neogi S. Three-body abrasive wear of short glass fiber polyester composite. Wear 2000;242:32-46.

[27] Cenna AA, Doyale J, Page NW, Dastoor P. Wear mechanisms in polymer matrix composites abraded by bulk solids. Wear 2000;240:207-214.

Effect of 8-13WT%Mn on the Microstructural Characterization of Fe-Mn-C Steel

Arnab Sarkar*[1], Prof. T. K. Bandhyopadhay[2]

*[1]Department of Metallurgical and Materials Engineering, Indian Institute of Technology, Kharagpur, Kharagpur-721302, India

[2]Department of Metallurgical and Materials Engineering, Indian Institute of Technology, Kharagpur, Kharagpur-721302, India

*[1]arnabandroid404@gmail.com; [2]tapas.ipr@gmail.com

Abstract

Mn based steels have shown promise for automotive application but however very limited research was conducted in medium Mn range that is aimed at enhancing the mechanical properties through microstructural control. Till now, it has been reported that both high and low Mn steel are undesirable for automotive application. Thus two different steel composition characterized as Fe-0.62C-13.64Mn-4.24Al-2.29Si, (S-1) and Fe-0.54C-8.36Mn-5.24Al-1.72Si, (S-2) produced by melting-casting route, have further been mechanically worked and heat-treated to obtain the desired microstructure. Microstructural analysis reveals austenite as the major phase along with martensite after quenching and tempering heat treatment. The steel containing higher Mn with low stacking fault energy results in hexagonally closed packed ϵ-martensite formation where as the steel containing lower Mn with relatively higher stacking fault energy results in body centered tetragonal α-martensite formation.

Keywords

Stacking Fault Energy; Microstructure; ε -martensite; α-martensite and Phase Fraction

Introduction

In the present 21st century, the different materials are available for automobile application. Steel has been the dominant material used in automotive industry since the 1st decade of the 19th century [1]. The current trend of the automobile sectors is to focus on the newer generation steel for producing not only the light weight vehicle for lesser fuel consumption but also to enhance the crash resistance property for providing safety to the passengers [1]. To meet the demands of these automotive sectors, Mn addition as the chief alloying element creates the greater impact in producing these newer generations steel [1]. The properties of these newer generation steel are derived from its microstructure. Generally, multiphase microstructure (mixture of ultra fined grained ferrite, martensite and austenite) can be obtained by optimizing the proper chemical composition as well as its heat treatment [2]. Much has been reported in the literature regarding the morphology and crystal structure of martensite within the austenitic matrix. However with respect to the medium Mn steel, it is very difficult to get martensitic structure due to the higher stability of the austenite [2, 3]. So the aim of the present work is to produce and characterize medium Mn steel with varying Mn content to see its effect on microstructure.

Experimental

The cast sample having 120*40*50mm dimension synthesized by melting-casting route was subsequently forged to 50%reduction after austenizing it above 1150°C for 2 hours. The forged samples were heat treated to reveal the two phase or multiphase microstructures.

Heat Treatment:-

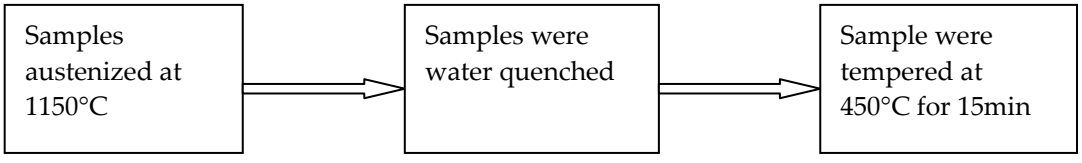

2226-4523/15/01 016-6 © 2015 DEStech Publications, Inc.
doi:10.12783/ijmsci.2015.0501.03

The basic aim of the heat treated sample (Quenching and Tempering) is to produce a desirable microstructure for optimum properties. These samples were examined under QUANTA FEG scanning electron microscope and FEI-TECHNAI G2 20S-TWIN transmission electron microscope to observe the detailed view of the microstructural features, morphology and also to measure the grain size. For phase detection of this cast, forged and heat treated samples, X-ray diffraction was done by using BRUKER'S D8 ADVANCED instrument. Furthermore, this XRD data were also used to determine the amount of phases present in each sample. To make the calculation of each phase easier we take the mathematical expression as

$$I_\gamma = K_2 R_\gamma C_\gamma / 2\upsilon \quad (1)$$

$$I_\alpha = K_2 R_\alpha C_\alpha / 2\upsilon \quad (2)$$

Dividing 1 and 2 we get,

$$I_\gamma / I_\alpha = (R_\gamma C_\gamma) / (R_\alpha C_\alpha) \quad (3)$$

Where as

I_γ= Integrated Intensity per unit length of the diffraction line of the austenite (γ) phase.

I_α= Integrated Intensity per unit length of the diffraction line of the martensite (α) phase.

I_γ and I_α are the integrated intensities which is the area under the curve after background subtraction.

C_γ and C_α= They represent the volume fraction of each of the phases respectively in the mixture and C_γ / C_α depends upon the ratio of the integrated intensity of the diffracted beams. The ratio of the integrated intensities depends on the R-values of the corresponding γ and α phase (as indicated from the table 1).

υ = linear absorption coefficient (m^{-1}) which enters as the absorption factor, 1/2 υ.

K_2 depends only on the incident beam not on the crystal structure [4].

TABLE 1. CHEMICAL COMPOSITION OF AS SYNTHESIZED STEEL.

Sample ID	C (wt %)	Mn(wt %)	Al(wt %)	Si(wt %)	Cr(wt %)	Fe(wt %)
S-1	0.62	13.64	4.24	2.29	0.046	79.16
S-2	0.54	8.36	5.24	1.72	1.14	83.14

Calculation of SFE

Thermodynamic model was used to determine the SFE of the developed material. Saeed Akbari et.al [5] calculates the SFE of fcc alloys, C, as follows:

$$\gamma_{SFE} = 2\varrho\Delta G^{\gamma\rightarrow\varepsilon} + 2\sigma^{\gamma/\varepsilon} + 2\varrho\Delta G_{ex}$$

where $\Delta G_i^{\gamma\rightarrow\varepsilon}$ is free energy change, due to hcp martensite formation from f.c.c austenite in pure metals. ϱ is the molar surface density along {111} planes and $\sigma^{\gamma/\varepsilon}$ is the γ/ε interfacial energy and ΔG_{ex} is excess free energy.

Result and Discussion

The chemical composition of as forged steel has been analyzed by using XRF and reported in Table 1.Synthesized steels designated as S-1 and S-2 are having Mn as the chief alloying element. Along with Mn, other alloying elements like Al, Si and Cr were also added which has the significant effect on the stacking fault energy of the steel (as shown in table 2). Moreover it has been reported both low as well as high Mn content in the steel are not suitable for automotive application. Low Mn content in the steel provides high strength but poor ductility where as high Mn content in the steel provides high strength and ductility but less corrosive resistive properties, poor machinability and even poor hot working above 1150 °C [1]. The main purpose of choosing such a composition is to obtain the desired microstructure, multiphase microstructure for getting optimum properties of the developed materials.

TABLE 2. SHOWING THE STACKING FAULT ENERY OF THE SYNTHESIZED STEEL.

Sample ID	Stacking fault energy (mJ/m²)
S-1	12.495
S-2	17.058

Effect of Composition and Stacking Fault Energy on Microstructure:-

Table 3 shows the volume fraction of various phases in heat-treated steel. It is revealed that higher content of Mn in sample S-1 stabilizes larger volume fraction of austenite [5,6]. So even after quenching and tempering treatment, high stability of austenite restrict the strain induced martensitic transformation. Saeed Akbari and Wolfgang Bleck [5] reported that the Mn content varying within 10-20 wt% shows the formation of austenite and (α+ε) martensite where as Mn content varying from 5-10 wt% shows the formation of austenite and α martensite. High content of fcc elements like Mn in developed material stabilizes the γ phase which tends to reduce the stacking fault energy of the alloy [5].

After the quenching and tempering condition, S-1 is having retained austenite and martensite in the final microstructure where as in S-2, there is the mixture of phases (ferrite, austenite and martensite) as depicted in figure 1(a) and 1(b). The presence of Mn as the chief alloying element stabilizes the austenite phase more than any other phase. So in all the conditions from the XRD data, austenite is reported to be the major phase in the microstructure. XRD pattern shown in figure 1 is interpreted in the microstructure of the heat treated samples.

TABLE 3. SHOWING THE VOLUME FRACTION OF RETAINED AUSTENITE IN HEAT TREATED STEEL.

Sample	I_γ/I_α	Temperature	R_γ/R_α	C_γ	C_α	%RET ϒ
S-1	25.442	20°C	1.12	0.957	0.0421	95.7%
S-1	21.00	20°C	0.35	0.978	0.029	97.8%
S-2	0.29	20°C	0.62	0.35	0.65	35%
S-2	0.60	20°C	1.12	0.335	0.665	33.5%

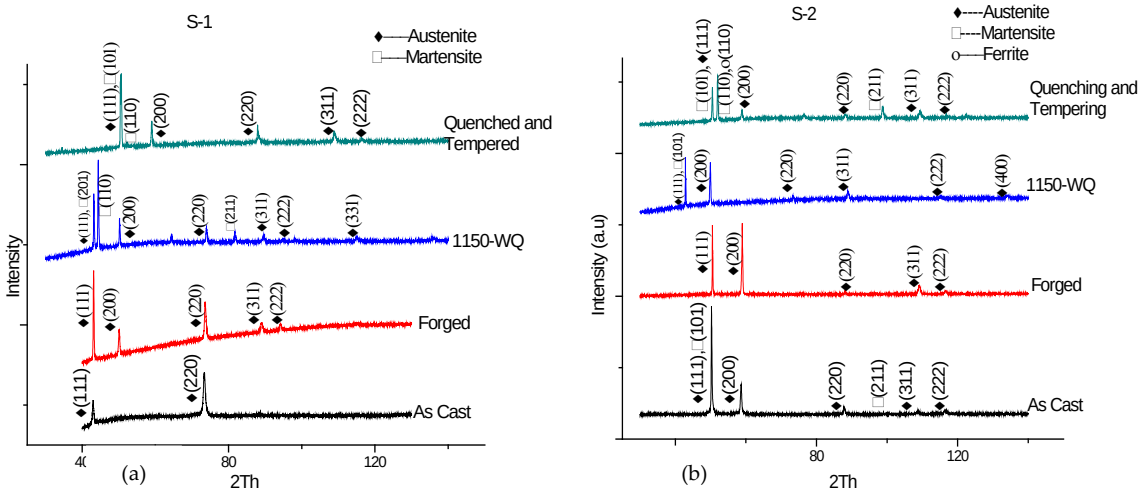

FIGURE 1. SHOWS THE XRD PATTERN OF A) S-1 AND B) S-2 AT DFFERENT CONDITIONS.

Figure 2 represents the microstructure of the heat-treated samples. The microstructure of S-1 mainly consists of ε-martensite within the austenitic matrix whereas the microstructure of S-2 contains α-martensite within the in austenitic matrix. Higher stability of austenite structure after the heat treatment exploit the plasticity induced transformation that may lead to formation of ε-martensite in S-1 within the austenitic matrix as shown in figure 2 (a) & (b) [6, 7]. Higher Mn content lower the stacking fault energy at room temperature (as shown in Table 2) that causes deformation occurs by twinning rather than by slip [8]. Formation of the wide stacking fault in austenite is accepted as the origin of ε or epsilon phase. The fcc structures deform by slip between the (111) plane. If the structures are in the series of ABCABC atomic arrangement, then slip between these planes results in ABCACAB

structures. So these so called stacking faults generate a hcp structures. With low stacking fault energy, epsilon martensite sometimes predominates in the microstructure . The stacking fault is the faulted region between two partial dislocations. These partial dislocations when present in large number cannot readily slip or pass one another and thus pile up and increases the work hardening rates [9]. Thus the high work hardening rate depends upon the stacking fault energy of the material and the magnitude of SFE controls the ease of cross slip and different deformation mechanism [2].

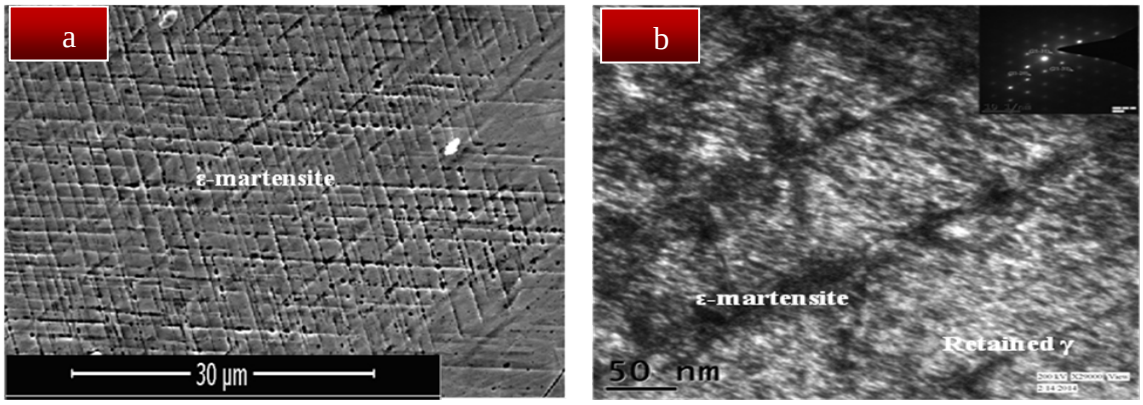

FIGURE 2. SHOWING THE a) SEM, b) TEM OF S-1 REVEALING THE ε-MARTENSITE FORMATION.

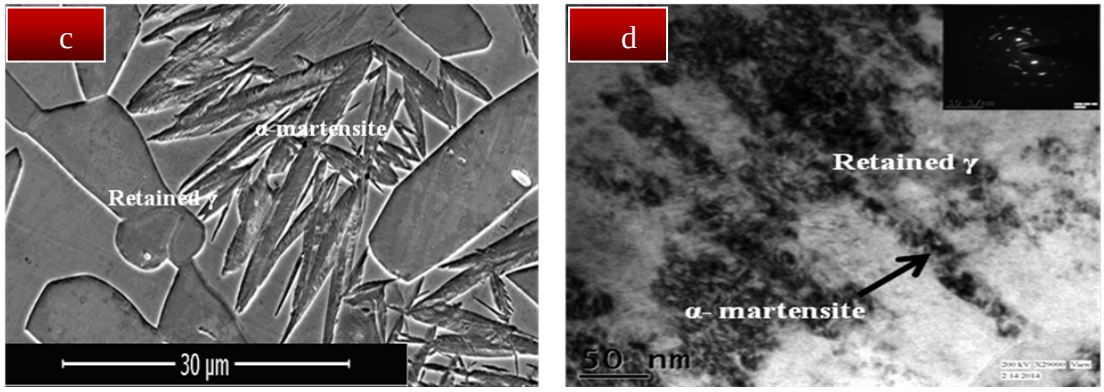

FIGURE 2. SHOWING THE c) SEM, d) TEM OF S-2 REVEALING THE α -MARTENSITE FORMATION.

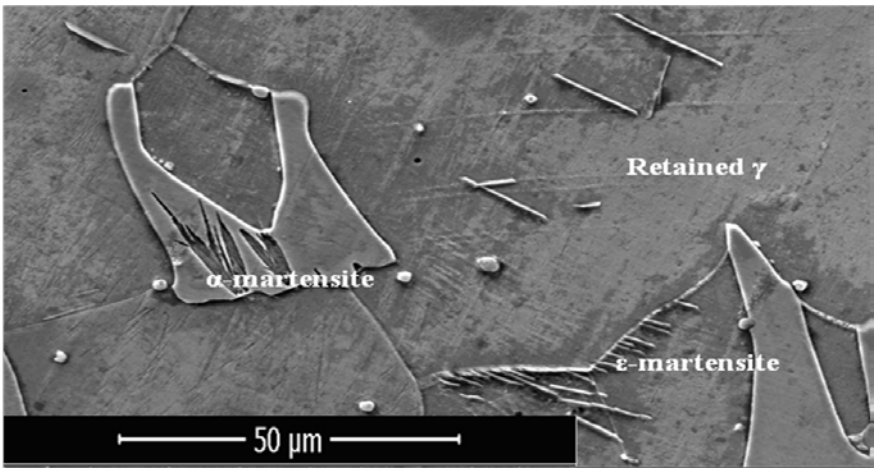

FIGURE 3. SHOWING THE TRANSFORMATION OF α-MARTENSITE BOTH FROM RETAINED AUSTENITE AS WELL AS FROM TWO STAGE TRANSFORMATION OF ε- α MARTENSITE.

In S-2, Mn content is comparatively lower than S-1. As the Mn content is within 5-10 wt% range, there is a formation of α-martensite within the austenitic matrix after quenching and tempering [5]. Due to the lower Mn content in S-2, deformation occurs mostly by slip mechanism which results in the formation of α-martensite as shown in figure 1 (c) and (d) [10,11]. Complete diffusionless transformation is occurring in S-2 results in the formation of body centered tetragonal lattice which has been termed as α-martensite. α-martensite occurs at the

preferred site: a) along sheets of faulted γ b) at the intersection of two ε bands or one ε band and another slip plane c) at the intersection of ε bands with grain or twin boundaries and d) at the intersection of two slip bands by the pile up of dislocations [12]. Lower Mn content in S-1 leads to the increase of the stacking fault energy but it is still <20mJ/m^2 (Table 2). Stacking Fault Energy varying within 10-20mJ/m^2 favors both α-martensite as well as ε-martensite formation The tetragonality and the volume of the martensitic plates increases with the increase in C content as shown in figure 2 (c) & (d). However in S-2 from α-martensite is not only formed from retained austenite but also during the two stage transformation from ε-α. as revealed in figure 3.

Effect of Stacking Fault Energy on Hardness:-

Moreover the low stacking fault energy in S-1 leads to the higher hardness as compared to S-2 in all the conditions (as shown in figure 4). After quenching and tempering, ε-Martensite formation in S-1 restrict the dislocation flow which thereby increases the hardness in the specimen. Thus S-1 is having higher hardness as compared to S-2.

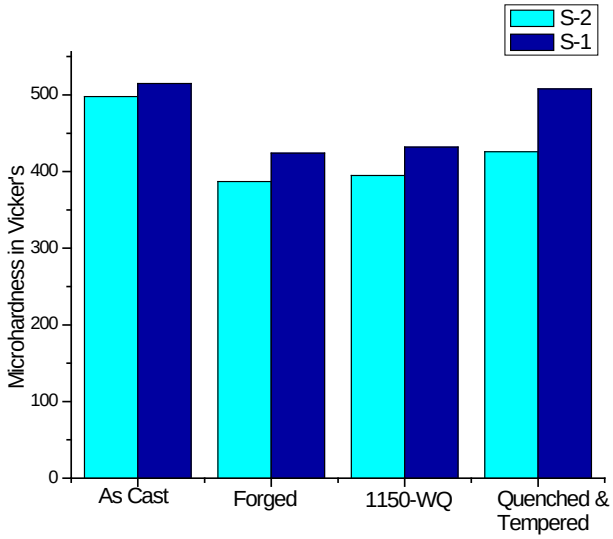

FIGURE 4. BAR CHART REVEALS THE HARDNESS VARIATION OF S-1 AND S- 2 AT VARIOUS CONDITION.

Conclusion

1) The higher Mn content in S-1 increases the austenitic volume fraction which thereby decreases the tendency for martensitic transformation after quenching and tempering.

2) Higher alloying leads to lower stacking fault energy. Stacking fault energy lying within 10-20 mJ/m^2 favors both the formation of ε-martensite and α-martensite. Deformation occurs both by slip and twinning results in the formation of ε-martensite in S-1. The cross-linked structure in S-1 decreases the dislocation flow during plastic deformation which thereby increases the hardness in S-1. Even it is expected that because of ε-Martensite formation, S-1 will have higher strength but poorer ductility than S-2.

3) But in S-2, diffusionless transformation occurs mostly by the slip which leads to the α-martensite formation within the austenitic matrix. However α-martensite formation not only takes place from retained austenite but also from two stage transformation of ε- α martensite. Hardness of S-2 is lower than S-1 but it is expected to have better ductility than S-1.

REFERENCES

[1] Grajcara, R.Kuziak , W. Zalecki. "Third generation of AHSS with increased fraction of retained austenite for the automotive industry." Archives of civil and mechanical engineering I2 (2012): pp.334-341.

[2] R. Kuziak, R. Kawalla and S. Waengler. "Advanced high strength steels for automotive industry." Archives of civil and mechanical engineering 8 (2008): 104-117.

[3] H.F.Xu, J.Xao and W.Q.Cao et.al. "Heat Treatment effects on the microstructure and the mechanical properties of a

medium manganese steel." Materials Science and Engineering A532 (2012): 435-442.

[4] B.D Cullity. "Elements of X-Ray Diffraction ." Third edition (2001).

[5] Saeed-Akbari, J.Imlau, U.Prahl and W.Bleck. "Derivation and variation in Composition-Dependant stacking fault energy maps based on subregular solution model in high Manganese steels." The minerals, metals and materials society and ASM International (2009):1-15.

[6] Huseyin Aydin, ElhachmiEssadiqi, In-HoJung and StephenYue. "Development of 3rd generation AHSS with medium Mn content alloying compositions." Materials Science & Engineering A564 (2013): 501-508.

[7] Sidney H.Avner. Introduction to Physical Metallurgy (2009), pp.349-387.

[8] Madeleine Durand-Charre. Microstructure of Steels and Cast Irons (2004): 213-219.

[9] Austenitic Stainless Steels. ASM International (2008): 1-10.

[10] Ludovic Samek and Daniel Krizan. "STEEL – MATERIAL OF CHOICE FOR AUTOMOTIVE LIGHTWEIGHT APPLICATIONS." Metal Review (2012): 1-6.

[11] George.E.Dieter. Mechanical Metallurgy (2009): 184-270.

[12] Ravi Kumar , A.K. Singh , B. Mahato , P.K. De, N.R. Bandyopadhyay , D.K. Bhattacharya. "Deformation-induced transformation textures inmetastable austenitic stainless steel." Materials Science and Engineering A429 (2006): 205–211.

Simulation of Organic Solar Cell at Different Active Layer Thickness

Narender Singh[1], Ashish Chaudhary[2] & Nikhil Rastogi*[3]

[1]Research Scholar, Department of Physics, School of Sciences, IFTM University, Moradabad, U.P. India

[2]Department of Physics, School of Sciences, IFTM University, Moradabad, U.P. India

[3]Department of Physics, School of Sciences, IFTM University, Moradabad, U.P. India

[1]nspal_physics@rediffmail.com; [2]mrashih32@gmail.com; [3]nr.cetiftm@gmail.com

Abstract

The J-V characteristics of organic hetero junction solar cell of different active layer thicknesses have been simulated by AMPS-1D software. A composite of P3HT: PCBM is used as photo active layer material, sandwiched between a transparent ITO electrode and Al back side contact. The simulation results clearly demonstrated that the dark J-V characteristics and electric field across the junction of hetero junction solar cell are affected by the active layer thickness.

Key Words

Organic Solar Cells; J-V Characteristics; AMPS-1D Software

Introduction

Organic solar cells based on conjugate polymers are much promising for a cheap and flexible alternative to inorganic solar cells. Nowadays many solar cell technologies exist in which organic solar cells are one of the newer classes of these technologies. Polymer based photovoltaic solar cells have attracted a lot of attention in the last decade due to their potential applications as flexibility, renewable, nonconservative energy sources. Since the discovery of photo induced charge transfer between organic donors and acceptors, a great effort has been devoted to explore these materials for photovoltaic applications [1–3]. Organic solar cells are now considered as important renewable energy sources that are alternative to their inorganic counterparts, for example, silicon photovoltaic cells [4]. An organic solar cell consists of an organic layer which possesses the basic steps in photovoltaic generation such as light absorption, charge carrier transport and extraction or injection of charge carrier through the contacts. P3HT (poly3-hexylphiophene) is a good electron donor material that effectively transports electrons. PCBM ([6, 6] – phenyl C_{61}-butyric acid methyl ester) is electron acceptor materials which transport electrons from molecule to molecule. P3HT: PCBM has reported the efficiency as high as 5% which is unusual in organic solar cell material. The performance solar cell has improved a lot in the last few years and the power conversion efficiency (η) of – 6.5 % has successfully been achieved in a tandem structure of ITO/ P3HT: PCBM/Al [5] solar cell. Recently, the progress on organic solar cell has moved forward on various frontiers, such as transparent and tandem or stacking structures to increase the efficiency [6-8]. An organic solar cell consists of organic active materials sandwiched between two metal electrodes forming two schottky junctions. If the two metal electrodes have different work functions, the Fermi level alignment develops an internal electric field known as built in electric field and the corresponding voltage developed at the two electrodes is known as the built in voltage. Depending upon the electrodes the built in voltage can be as high as $\sim$ 1.3V in organic solar cell [9]. Monester [10] has observed this trend based on P3HT: PCBM devices. In their experiments, the active layer thickness is varied from few tens nanometer to 215 nm. When thickness is 70nm, J_{sc} reaches the maximum value followed by a little decrease until 140nm. When the thickness increases, further J_{sc} increases again. There is the deviation between the prediction and the experimental results as shown in figure 1. In this paper we have study the effect of active layer thickness on the dark J-V characteristics and electric field across the junction for ITO/P3HT: PCBM/Al solar cell.

2226-4523/15/01 022-5 © 2015 DEStech Publications, Inc.
doi:10.12783/ijmsci.2015.0501.04

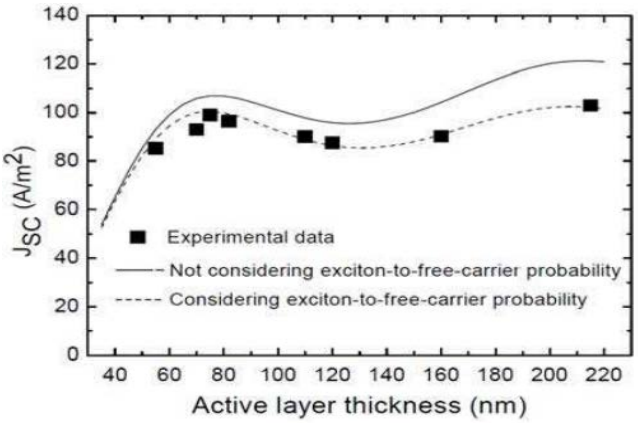

FIGURE 1. THICKNESS DEPENDENCE OF SHORT CIRCUIT CURRENT

Simulation

FIGURE 2. ITO/P3HT: PCBM/Al SOLAR CELL

The simulation of ITO/ P3HT: PCBM/Al solar cells have been done at different thicknesses of active layer (taking equal thickness of P3HT & PCBM layer) using AMPS-1D software (figure 2). The calculations are carried out using AMPS-1D for analysis which is based on Poisson's equations and first principle continuity equation of electrons and holes [11] and used to analyze the carriers transport behavior of organic semiconductor electronic device structures including solar cells. Poisson's equation links free carrier populations trapped charge populations and ionized dopent populations to the electrostatic field presented in material system. One dimensional Poisson's equation is given by

$$\frac{d}{dx}\left[-\epsilon(x)\frac{d\psi}{dx}\right] = q^{*}[p(x) - n(x) + N_D^{+}(x) - N_A^{-}(x) + p_t(x) - n_t(x)]$$

where Ψ is electrostatics potential, n free electrons, p free holes, n_t trapped electrons , p_t trapped holes, N_D^+ and N_A^- are ionized donor like doping concentrations and acceptor like doping concentrations and they are all the functions of the x. Here □is the permittivity and q is the magnitude of charge of electron. The continuity equations for the free electrons and holes in the delocalized states of the conduction band and valence band respectably have the form

$$\frac{1}{q}\left(\frac{dJ_n}{dx}\right) = -G_{op}(x) + R(x) \qquad \text{for electron}$$

$$\frac{1}{q}\left(\frac{dJ_p}{dx}\right) = G_{op}(x) - R(x) \qquad \text{for hole}$$

where J_n and J_p are, respectively, the electron and hole current densities. The term R(x) is the net recombination rate resulting from direct band-to-band recombination and indirect Shockley-Read-Hall (SRH) recombination through gap (localized) states and the term $G_{op}(x)$ is the optical generation rate as a function of x due to externally imposed illumination.

In AMPS-1D, the user has the choice of two different models, one is the density of states (DOS) model, and the other is the life time model. In DOS model the details of recombination traffics trapping and the charge state of the

defects are fully accounted, because of all the recombination traffics, trapping, re-admission etc, and their effects on the electric field in the DOS model, and this approach requires that the user input the energy gap distribution of the defects as well as spatial variation. This approach also requires capture cross–section information to quantity the attractiveness of the various defects to electrons and holes. In this paper, we use the DOS model for the simulation of the ITO/ P3HT: PCBM/Al solar cell.

Parametric Equations Required for Simulation at Temp. 300k

Ban gap [12] in eV $E_g(x) = 0.7x + 3.4(1-x) - 1.43(1-x)$

where x is the mole fraction.

Absorption coefficient (13) in μm^{-1} $\alpha(\lambda E_g) = A\sqrt{\frac{1.2398}{\lambda} - E_g}$

Where λ is the wavelength in μm and $A = 2.2 \times 10^5\ \mu m^{-1}(eV)^{-1/2}$

Electron affinity [13, 14] in eV

$$\chi(E_g) = 4.1 + 0.7(3.4 - E_g)$$

Relative Permittivity [14]

$$\varepsilon_r(x) = 14.6x + 10.4(1-x)$$

The effective density of states in the conduction band and valence band respectively in cm^{-3} is,

$$N_c(x) = 0.9x + 2.3(1-x)$$

And

$$N_V(x) = 1.3x + 1.8(1-x)$$

Carrier mobility [15] in $cm^2V^{-1}s^{-1}$

$$\mu_i(N) = \mu_{min,i} + \frac{\mu_{max,i} - \mu_{min,i}}{1 + \left(\frac{N}{N_{g,i}}\right)^{\gamma_i}}$$

where i = n, p denotes electrons and holes respectively and N is doping concentration, while the model parameters $\mu_{max,i}$, $\mu_{min,i}$, $N_{g,i}$ and γ_i depend on the type of semiconductor [8].

TABLE 1. PARAMETERS FOR THE SIMULATION OF ITO/ P3HT:PCBM/Al SOLAR CELL

Layer	Dielectric constant (EPS)	Electron mobility (MUN) Cm²/V/s	Hole mobility (MUP) Cm²/V/s	Conduction band effective density of state(NC) Cm³	Valence band effective density of state (NV) Cm³	Number of acceptor (NA) /Cm³	Number of donors (ND) /Cm³	Energy band gap (EG) eV	Electron Affinity (CHI) eV
P3HT	3.4	1.0e-4	1.0e-3	1e+22	1e+22	----------	3.17e+13	1.85	3.1
PCBM	3.0	1.0e-3	1.0e-4	1e+22	1e+22	3.17e+13	--------	2.1	3.7

Result & Discussion

In this paper, ITO/ P3HT: PCBM/Al solar cells of different active layer thicknesses are designed. The dark J-V characteristics and electric field across the junction are simulated for different active layer thicknesses. The figure3 shows the dark J-V characteristics of P3HT: PCBM solar cells for different active layer thicknesses of 100nm, 150nm, 200nm and 300nm. It is observed that as the active layer thickness increases the dark current decreases except for 150 nm. For 200nm, 300nm the dark current curves are smooth. Dark I-V measurements are used to inject carriers into the circuits with electrical means rather than light generated carriers. The variation of electric field across the junction for active layer thickness of 100nm, 150nm, 200nm and 300nm is shown in figure 4.

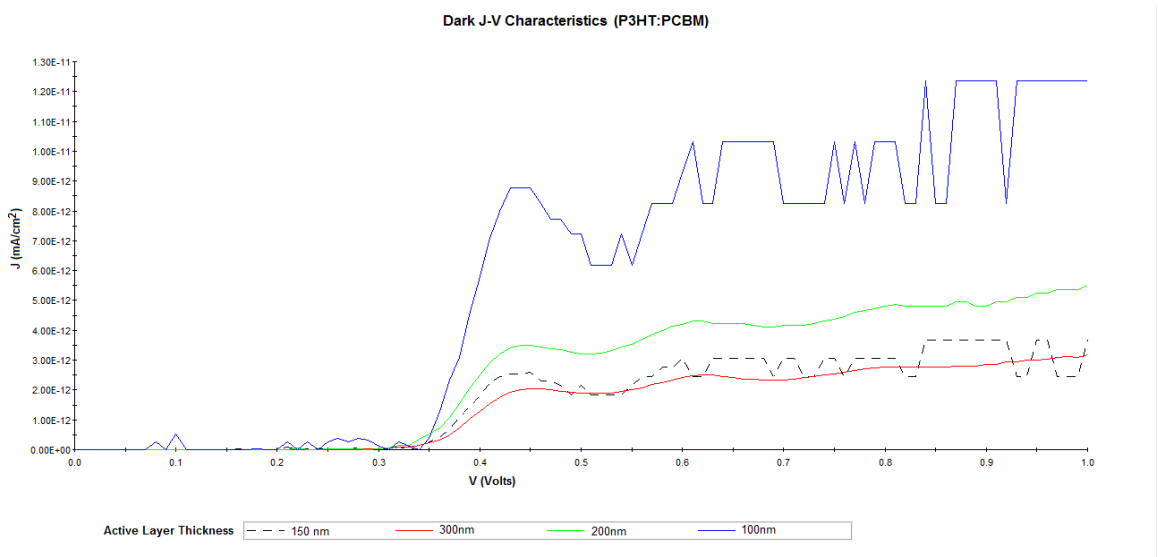

FIGURE 3. VARIATION OF DARK CURRENT FOR DIFFERENT ACTIVE LAYER THICKNESS

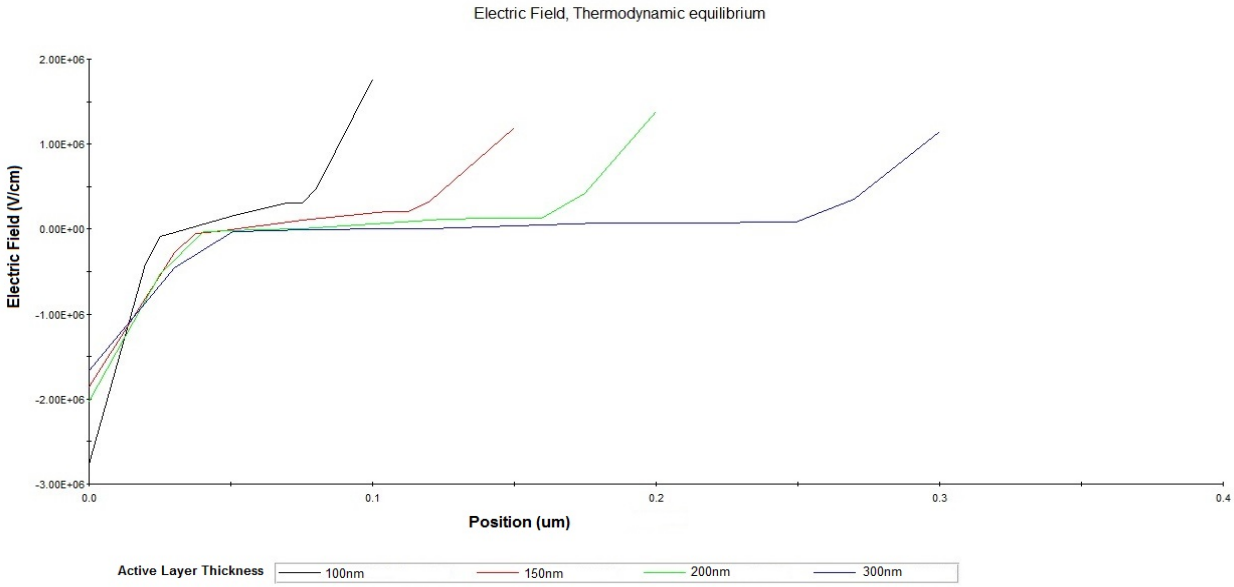

FIGURE 4. VARIATION OF ELECTRIC FIELD ACROSS THE JUNCTION FOR DIFFERENT ACTIVE LAYER THICKNESS

Conclusion

The optical performance of the P3HT: PCBM solar cell is simulated by AMPS-1D to study the J-V characteristics and electric field with active layer thickness. The dark current changes with the increase in active layer thickness of the used material in the process. We get smooth J-V characteristics curves for 200nm, 300nm. The electric field across the junction also changes with active layer thickness. The electric field decreases as the active layer thickness increases. The electric field across the junction decreases as active layer thickness increases. Thus AMPS-1D may be used to study the performance of organic solar cells.

ACKNOWLEDGEMENT

The authors are thankful for Department of Physics, School of Sciences, IFTM University, Moradabad, UP, India for providing the necessary research facility as well as the support to complete the research paper.

REFERENCES

[1] N. S. Sariciftci, L. Smilowitz, A. J. Heeger, and F. Wudl, Science 258, 1474, 1992.

[2] G. Yu, J. Gao, J. C. Hummelen, F. Wudl, and A. J. Heeger, Science 270, 1789, 1995.

[3] N. Rastogi, N. Singh and M. Saxena, "A brief review on current need of organic solar cells" International Journal of Innovative Research in Science, Engineering and Technology, Vol. 2, Issue 12, December 2013

[4] W. D. Johnston, Jr., Solar Voltaic Cells, Dekker, New York, 1980.

[5] J. Y. Kim, K. Lee, N. E. Coates, D. Moses, T. Q. Nguyen, M. Dante, and A. J. Heeger, Science 317, 222, 2007.

[6] V. Shrotriya, E. H. Wu, G. Li, and Y. Yang, Appl. Phys. Lett. **88**, 064104, 2006.

[7] G. Li, C.-W. Chu, V. Shrotriya, J. Huang, and Y. Yang, Appl. Phys. Lett. **88**, 253503, 2006_.

[8] A. Hadipour *et al.*, Adv. Funct. Mater. **16**, 1897 _2006.

[9] F. Monestier, J. J. Simon, P. Torchio, L. Escoubas, F. Flory, S. Bailly, R. Bettignies, S. Guillerez, & C. Defranoux, Modeling the short-circuit current density of polymer solar cells based on P3HT:PCBM blend Solar cell.

[10] V. D. Mihailetchi, P. W. M. Blom, J. C. Hummelen, and M. T. Rispens, J.Appl. Phys. **94**, 6849 _2003.

[11] S. Fonash, et al., *http://www.cneu.psu.edu/amps.*

[12] Wu, J., Walukiewicz, W., Yu, K. M., Ager III, J. W., Haller, E. E., Lu, H., Schaff, W. J., Saito, Y. and Nanishi, Y., "Unusual properties of the fundamental band gap of InN," *Appl. Phys. Lett., 80*, 2002, 3967-3969.

[13] Xiaobin Zhang et al, "Simulation of In0.65Ga0.35 N single-junction solar cell" *J. Phys. D: Appl. Phys., 40*, 2007, 7335–7338.

[14] M. E. Levinshtein, S. L. Rumyantsev, and M. S. Shur, *Properties of Advanced Semiconductor Materials*, (Wiley, Chichester, UK, 2001, 1–90).

[15] T. T. Mnatsakanov, M. E. Levinshtein, L. I. Pomortseva, S. N. Yurkov, G. S. Simin, and M. Asif Khan, "Carrier mobility model for GaN" *Solid-State Electron. 47*, 2003, 111-115.

Biography

Mr. Narender Singh did Master in Physics (Electronics) from MJP Rohilkhand University, Bareilly, UP and M.Phil. from Singhaniya University Rajasthan, and he is a research scholar in the department of Physics, School of Sciences, IFTM University, Moradabad. His area of research is solar Cell & nano technology.

Mr. Ashish Chaudhry did Master in Physics (Electronics) from HNB Garhwal University, UK, India. He has submitted Ph.D. thesis in Physics at R.M.L. Awadh University, Faizabad, UP, India. His area of research is nanotechnology, material science and electronics. He is working as Assistant Professor in the department of Physics, IFTM University, Moradabad, UP, India. He has published 5 papers in national journal of repute.

Dr. Nikhil Rastogi is a Master in Physics (Electronics) and Doctorate in Solid State Physics from M.J.P. Rohilkhand University, Bareilly, UP, India. He has overall 14 years of quality teaching experience in Physics at both UG and PG level. His active engagement in research area spans across ten years. His membership includes professional bodies like IAS, ISC & IPA and is an active member of editorial board of many national/international journals in the areas of Materials Science, Sensors and Semiconductor. He has published more than 20 research papers in national and International journal of repute.

A Unified Model of Crack Propagation in Scratched and Unscratched Samples of Al 2024-T3 Clad

Nader A. Nader

Mechanical Engineering Department, Prince Mohammad Bin Fahd University, Kingdom of Saudi Arabia

nnader@pmu.edu.sa

Abstract

An experimental study of the effect of scratches on the fatigue life and fatigue crack growth of Al 2024-T3 clad material has been conducted. The result showed that Al 2024-T3 clad material is a scratch sensitive material. It presented a significant drop in fatigue life, 95% with a scratch depth of 100 μm in comparison with the unscratched material. Also, it has been found that cracks propagate faster in scratched samples than unscratched and at a lower stress intensity factor. A model that predicts the fatigue crack propagation of scratched samples is proposed. Furthermore, scanning electron micrographs showed microcracks, generated by the presence of scratches, responsible in decreasing the fatigue life of the material.

Keywords

Crack Propagation Model; Scratched Samples; Fatigue Model

Introduction

Usually the relation describing the propagation of a fatigue crack in metals is presented in a logarithm plot of the crack propagation plot of the crack growth rate (da/dN) against change in stress intensity factor, ΔK, at the crack tip [1], (Figure 1). The lower limit or threshold, region I, shows the fatigue conditions under which the crack does not propagate. The upper limit, region III, covers the crack propagation associated with the start of final rupture. Region II is described by da/dN in Figure 1 for metals known as the Paris equation, [1] which has the form,

$$\frac{da}{dN} = C(\Delta K)^n \tag{1}$$

Where C, and n are numerical constants and a is the crack length. ΔKcan be expressed in terms of the geometry, stress and crack size [1], as

$$\Delta K = Y\Delta\sigma\ (a)^{1/2} \tag{2}$$

Another particular fracture mechanics parameter, ΔK_{th}, is known as the threshold stress intensity range (fatigue threshold). In order to study the crack growth of the material, linear elastic fracture mechanics theory (LEFM) has been applied to fatigue. This concept offers, at least in principal, a relation for stress magnitude and distribution near the crack tip to the remote stress, crack size, shape, and material properties of the cracked sample [2].

Region I in Figure 1 is used quite commonly in failure analysis. A number of investigators [3] have proven that cracks less than 1mm in length tend to show faster growth rates and lower threshold than long cracks. The growth of short cracks in aluminum alloys had been investigated by researchers [4]. Microcracks are formed near the intrusions in stage one of the crack growth. The crack tendency to grow at intrusions rather than slip bands depends on stress level and inclusion content. In addition, investigators [4] suggested that a slip band crack generally occurs from high stresses and higher purity of the alloys.

Pearson [5] concluded that crack size of approximately the average grain-size, grew faster than long cracks at identical ΔK values where ΔK is the range stress intensity factor and is defined as,

$$\Delta K = K_{max} - K_{min}.$$

Several models had been proposed to study the mechanisms of short crack under plane stress conditions. El

2226-4523/15/01 027-6 © 2015 DEStech Publications, Inc.
doi:10.12783/ijmsci.2015.0501.05

Haddad [6], suggested that $\Delta K_{th} = (\pi a + l_0)^{1/2}$, (l_0 is the effective crack length considering the small crack behavior), in which the standard equation for ΔK is modified by adding a constant, l_0, to the crack length. This equation fulfills the basic requirements in that it tends to a constant value at very short crack lengths, equal to the fatigue limit, and it merges with the long crack line once crack length becomes large compared to l_0.

The stress intensity factor equation was developed for cracks growing from notches in an infinite plate. For crack growing from the tip of an elliptical notch K_I was expressed as,

$$K_I = K_t\sigma\sqrt{\pi a} \tag{3}$$

where K_t is the stress concentration factor [7]. The local stress near the tip of the notch is elevated by the stress concentration. Dowling [8], used Eq. 3 to derive an expression for the transition crack length in short crack problem. For a short crack, a careful attempt should be made to control a relatively high stress for a given value ΔK value. If the stress is too high, LEFM conditions will fail and this will result in a larger plastic zone and faster crack propagation [9].

There have been several studies of fatigue crack initiation in Al 2024-T3 aluminum alloys. All studies found that fatigue cracks formed at the edges of the deformation bands due to intrusions or extrusions which formed there. These cracks grew and linked up with cracks in neighbouring grains thereby forming the fatal crack [17].

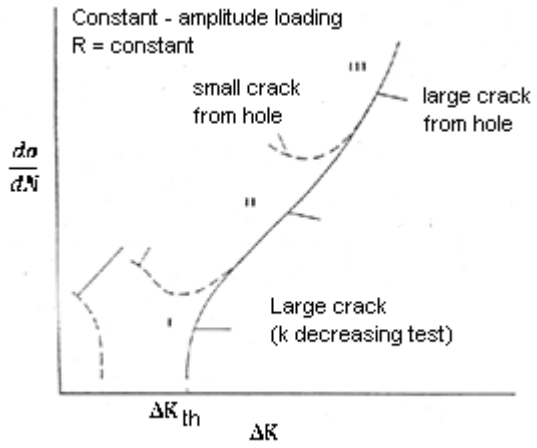

Figure 1 Typical fatigue-crack growth rate data for small and large cracks [3]

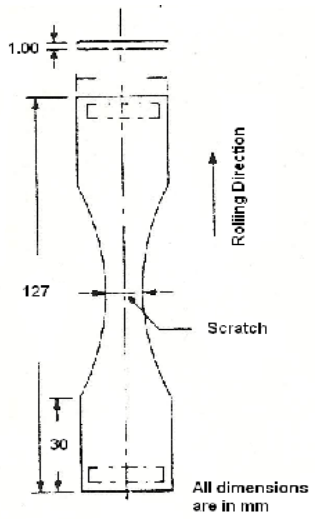

Figure 2 The configuration of fatigue specimen

Experimental Procedure

Fatigue Test Sample Preparation: Fatigue samples were cut from commercial grade 2024-T3 clad of 1.0 mm in thickness according to ASTM standards as shown in Figure 2 (scratch with a tip radius of 83 μm). Scratches were introduced on the samples across the width at the mid portion of the specimen. Once the scratch was introduced into the samples, the scratch depth was measured under the optical microscope. The technique consisted of focusing on the surface of the samples which was taken as reference point and then focusing on the scratch bed. The distance between these two points can be reliable and accurate with an acceptable error of +/- 1 micron.

Fatigue Crack Propagation Test Samples: Fatigue crack samples were polished using a standard polishing technique. A small scratch was introduced at the edge and through thickness of the samples for the startup of the crack. Crack propagation rate was made by observing the movement of the edge crack tip on the polished face with a traveling microscope. The thickness and width for all the fatigue crack propagation samples were 1 mm and 25.4 mm respectively. The calculations of stress intensity for scratched and unscratched samples were based on edge crack formula [10]:

$$K = Y\sigma\,(a)^{1/2}$$

Where

$$Y = 1.99 - 0.41\frac{a}{w} + 18.7\left(\frac{a}{w}\right)^2 - 38.48\left(\frac{a}{w}\right)^3 + 53.85\left(\frac{a}{w}\right)^4$$

Discussion

Crack Propagation: In applying the Paris law model, Eq. (1), and introducing the stress concentration factor (K_t), da/dN can then be written as:

$$\frac{da}{dN} = C(\Delta K_{eff})^n \tag{4}$$

Where,

$$\Delta K_{eff} = YK_t\Delta\sigma\sqrt{a} \tag{5}$$

K_t was obtained using the notch sensitivity factor equation, q, as

$$q = \frac{K_f - 1}{K_t - 1} \tag{6}$$

As defined [11], values of q range from zero (no notch effect) to unity (full theoretical effect). Through correlation to experimental data, a number of researchers had proposed analytical relationships for the determination of q. The most common is being proposed by Peterson [12] and Neuber [13]. Peterson showed the relationship q as a function of the notch tip radius (r, in inches),

$$q = \frac{1}{1+\frac{\beta}{r}} \tag{7}$$

For aluminum alloys β = 0.025, [14]. K_f which is defined as the fatigue stress limit, was taken as the ratio of endurance limit of unscratched to endurance limit of the scratched samples. Therefore in finding an equation for the fatigue crack growth for scratched samples, the ΔK_{eff} which counts for K_t has to be taken into consideration. Since it was shown earlier that the fatigue crack growth (da/dN) increased significantly as the scratch depth (d) increases, it is evident that the scratch depth with the tip radius influences the correction factor K_t. Hence combining Eq. (6) and (7), an expression for K_t is obtained as,

$$K_t = \left(K_f - 1\right)\left(1 + \frac{\beta}{r}\right) + 1 \tag{8}$$

Using the crack propagation data for unscratched samples (K_t =1) and Eq. 4, the material constant, c=4.41x10 $^{-10}$ and n=2.53, were obtained. Keeping C and n constant, Eq. 4 was used for the scratched samples. The following table shows the values obtained on computing K_t using Eqs.6, 7, and 8.

Table 1

Scratch depth, d [μm]	0	40	70	100	150
Endurance limit, S_e [MPa]	159	156	152	145	126
Fatigue stress limit, K_f	1	1.017	1.045	1.095	1.26
Stress concentration, K_t	1	1.16	1.41	1.86	3.4
Scratch sensitivity, q	0	0.11	0.11	0.11	0.11

To predict the growth rate of a small crack and in turn the fatigue life of structures containing short cracks, a method is needed that reflects ΔK_{eff} at the tip of short cracks. Mazumdar used an alternate approach in which he considered the microcracks interaction [15]. Convincing evidence [16] showed that the average crack spacing, in smooth specimens, initially decreases due to continued nucleation of microcracks. A fatal crack develops once this crack spacing with cycling assumes a steady state value when life is almost near exhaustion. Using this approach, Mazumdar derived a stress-life model for crack initiation in terms of some fundamental parameters,

$$\left[\left(\frac{\sigma}{\sigma_f}\right)^2 - 1\right]N_i = \left(\frac{D}{b}\right)\left(\frac{s}{s_f}\right) \tag{9}$$

The crack spacing ratio (s/s_f) which varies between 0 and 1, is an important element of this equation. A smaller ratio implies the presence of an increased crack population. Whereas, for a ratio of one crack densities are independent of stress or load. As this ratio could not be determined due to experimental difficulties, an indirect

approach would be to obtain the best fit of Eq. (9) to the experimental life data in the high cycle regime (Figure 3). As shown in Figure 3, there is a good agreement between the predictions and the life data of both unscratched as well as scratched samples containing 100μm, 150μm, and 225μm deep scratched. With the presence of deeper scratches, the ratio s/s_f would decrease to the minimum value. To compute the crack spacing ratio s/s_f, a relation was needed as a function of scratch depth. Weibull distribution was used in Figure 4 which fitted the actual values obtained as

$$\frac{s}{s_f} = exp\left[-\left(\frac{d}{\theta}\right)^{\alpha}\right] \tag{10}$$

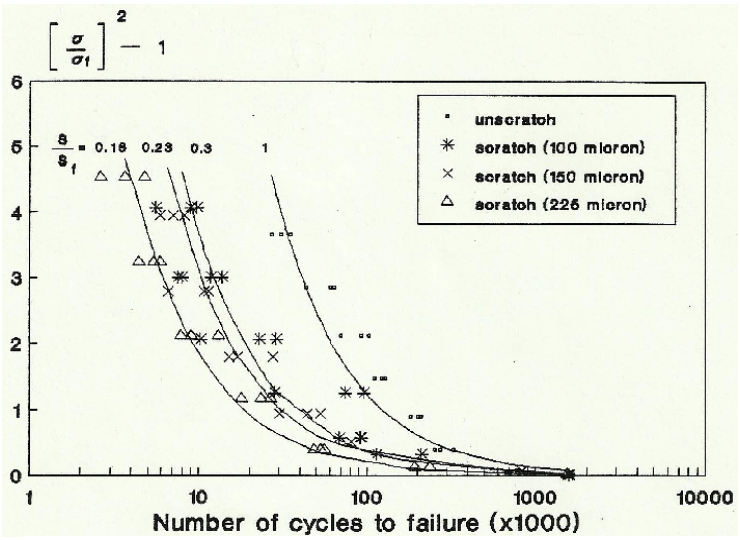

Figure 3 prediction of fatigue short cracks using crack spacing ratio s/s_f

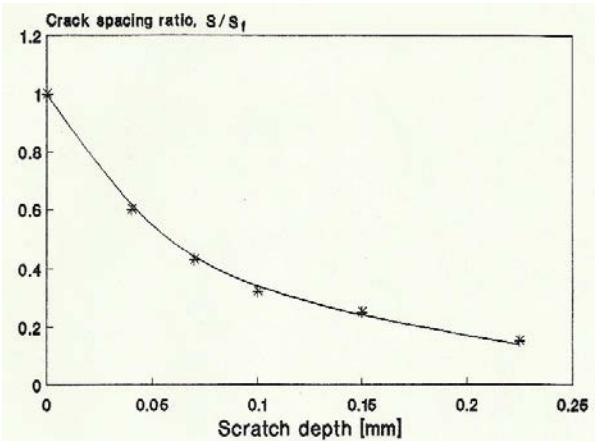

Figure 4 Crack spacing s/s_f as afunction of scratch depth

The relation can be better understood as the probability to find an area without a crack generated by the scratch. As the ratio decreases, the area (where non crack exists) decreases and thereafter the life of the scratched material is reduced. This is not unreasonable and, thus, as an initiator for microcracks behind it. In addition, microscopic examination of the scratched tip area, (for example, sample of 100 μm deep scratched fatigue at regular intervals) revealed the development of first surface microcracks around 10^4 cycles, Figure 5. Continuous examination of the scratched surface, showed also the presence of additional microcracks besides the growth of some existing ones.

In comparing the results obtained for short cracks using Eq. (9) to da/dN results, several steps have to be taken. First, solving for σ from Eq. (9) gives,

$$\sigma = \left[\sqrt{\frac{\left(\frac{D}{b}\right)\left(\frac{s}{s_f}\right)}{N_i} + 1}\right]\sigma_f \tag{11}$$

where σ is the stress amplitude required for crack initiation. Second, rearranging for ΔK in Eq. (4) as,

$$\frac{da}{dN} = c\left(\left(YK_t\Delta\sigma\sqrt{a}\right)\right)^n \tag{12}$$

And knowing $\Delta\sigma = \sigma_{max} - \sigma_{min}$, and $R = \sigma_{max} / \sigma_{min}$, then Δσ becomes,

$$\Delta\sigma = \sigma_{max}(1 - R) \tag{13}$$

Where σ_{max} is the same as σ in Eq. (11).Third, combining Eqs. (11) and (13), and substituting for Δσ in Eq. (12), da/dN would be obtained as,

$$\frac{da}{dN} = C(\Delta K_{scratch})^n \tag{14}$$

Where,

$$\Delta K_{scratch} = YK_t\left[\sqrt{\frac{\left(\frac{D}{b}\right)\left(\frac{s}{s_f}\right)}{N_i}+1}\right]\sigma_f(1-R)\sqrt{a}$$

Hence Eq. (14), of Paris equation form, indicates that for a short crack da/dN is a complex function of several factors geometry factor (Y), stress loading, $\sigma = f(d, N_i)$, and crack length (a). Figure 6 shows a good agreement of the predicted values of both short (Eq. 14) and long crack (Eq. 4) compared to the experimental results. A careful examination of the development of microcracks must be considered (N_i) and compared with Mzumdar model, before any attempt to predict da/dN values using Eq. (12).

Figure 5 Microcracks initiation at 10 cycles

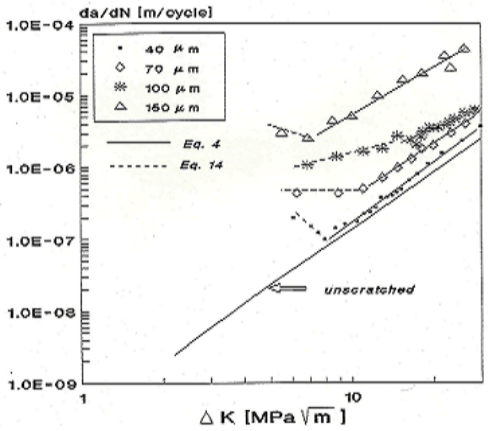

Figure 6 Models predictions of fatigue specimen

Conclusions

This study showed that Al 2024-T3 clad is a scratched sensitive material. As the scratch depth increased, the fatigue life of the material decreased significantly. Scratched samples generated microcracks which propagated at higher rates than unscratched samples and at lower stress intensity factor. Using the experimental data, simple models of the form of Paris equation were developed to predict both the short and long crack propagation in scratched samples.

REFERENCES

[1] P. C. Paris and F. Erdogan, "A critical Analysis of Crack Propagation Laws, " Trans. ASME, J.Basic Eng., Vol. D85, 1963, pp. 528-534

[2] Smith, Fatigue Crack growth 30 Years of Progress Ed., University of Cambridge, UK, Ed.Pergamonpress, (1986).

[3] J.C. Newman, Jr., M. H. Swain, and E. P. Phillips, "An Assessment of the Small-Crack Effectfor Al 2024-T3," Small Fatigue cracks, "Proc. Of the Sec. Eng. Found. Int. Conf. /Workshop, Santa Barbara California, (1986).

[4] J. Lankford, (1983).Fat.Eng. Mats.And Strcut. 6, 15-32

[5] S. Pearson, (1975). Eng. Frac. Mech. 7, 235-247.

[6] M. H. El Haddad, N. F. Dowling, T. H. Topper, and K. N. Smoth, (1980) International Journalof Fracture, 16, 15.

[7] J. M. Bransom, and S. T. Rolfe, Fracture & Fatigue Control in Structures, 2nd Edition, P. 42

[8] N. E. Dowling, 'Fatigue at Notches and the Local Strain and Fracture Mechanics Approaches," in Fracture Mechanics, ASTM STP 677, C. W. Smith (ed.), American Society for Testing and Materials, Philadelphia, 1979, pp. 247-273

[9] D. Taylor, "Fatigue Thresholds", p. 139, 1989.

[10] D. Broek, Elementary Engineering Fracture Mechanics, 4th Edition. 1986, p. 85.

[11] J. A. Bannantine, J. J. Corner, and J. L. Handrock, Fundamentals of metals Fatigue Analysis, 1990, pp. 126.

[12] R. E. Peterson, "Relation between Life testing and Conventional tests of Materials, "Bulletin ASTM No. 133, Mar. 1945.

[13] H. Neuber, Theory of Notch Stresses: Principal for Exact Stress calculations, Edwards, Ann Arbor, Mich., 1946.

[14] G. Sines, J. L. Waisman, Metal Fatigue, 1959, pp. 300-302.

[15] P. K. Mazumdar; A model for High Cycle fatigue; Engineering Fracture Mechanics, 1992.

[16] B. T. Ma and C. Laird; ActaMetallurgica 37 (1989) 349.

[17] C.Y. Kung and M. E. Fine, Fatigue Crack initiation and Microcrack Growth in 2024-T4 and 2124-T4 Aluminum Alloys, Metallurgical Transaction, Volume 10, 1979